

New insights on Stephan's Quintet: exploring the shock in three dimensions[★]

J. Iglesias-Páramo^{1,2}, L. López-Martín^{3,4}, J.M. Vílchez¹, V. Petropoulou¹ and J.W. Sulentic¹

¹ Instituto de Astrofísica de Andalucía (CSIC), Glorieta de la Astronomía s.n., 18008 Granada, SPAIN
e-mail: jiglesia@iaa.es, jvm@iaa.es, vasiliki@iaa.es, sulentic@iaa.es

² Centro Astronómico Hispano Alemán, C/ Jesús Durbán Remón, 2-2, 04004 Almería, SPAIN

³ Instituto de Astrofísica de Canarias, C/ Vía Láctea s.n., 38200 La Laguna, SPAIN
e-mail: luislm@iac.es

⁴ Departamento de Astrofísica, Universidad de La Laguna, E-38205 La Laguna, Tenerife, SPAIN

Preprint online version: August 6, 2018

ABSTRACT

Aims. In this paper we study the ionized gas emission from the large scale shock region of Stephan's Quintet (SQ).

Methods. We carried out IFU optical spectroscopy on three pointings in and near the SQ shock. We used PMAS on the 3.5m Calar Alto telescope to obtain measures of emission lines that provide insight into physical properties of the gas. Severe blending of H α and [NII] λ 6548,6583Å emission lines in many spaxels required the assumption of at least two kinematical components in order to extract fluxes for the individual lines.

Results. Main results from our study include: (a) detection of discrete emission features in the new intruder velocity range 5400-6000 km s⁻¹ showing properties consistent with HII regions, (b) detection of a low velocity component spanning the range 5800 – 6300 km s⁻¹ with properties resembling a solar metallicity shocked gas and (c) detection of a high velocity component at \approx 6600 km s⁻¹ with properties consistent with those of a low metallicity shocked gas.

Conclusions. The two shocked components are interpreted as products of a collision between NGC 7318b new intruder and a debris field in its path. This has given rise to a complex structure of ionized gas where several components with different kinematical and physical properties coexist although part of the original ISM associated with NGC 7318b is still present and remains unaltered. Our observations suggest that the low velocity ionized component might have existed before the new intruder collision and could be associated with the NW-LV HII component of Williams et al. (2002). The high velocity ionized component might fill the gap between the HII complexes observed in SQ-A and NGC 7319's tidal filament (NW-HV, Arc-N and Arc-S in Williams et al. 2002).

Key words. galaxies: interactions – galaxies: ISM – galaxies: groups: individual (HCG92, Stephan's Quintet)

1. Introduction

Stephan's Quintet (SQ) is one of the most spectacular and intriguing galaxy systems in the local Universe. Discovered by Stephan in 1877 it has become a "Crab Nebula" in extragalactic astronomy as the subject of a multitude of studies across the electromagnetic spectrum. It was known since the 60s that one of the galaxies - NGC 7320 - shows a highly discordant redshift (Burbidge & Burbidge 1961) that converted it from a quintet into a quartet. It has long since regained quintet status with the discovery of two tidal tails extending toward accendant redshift galaxy NGC 7320c (Arp 1973). A dynamical analysis revealed that SQ consists of a core of three galaxies that have experienced several episodes of dynamical harassment from an "old intruder" NGC 7320c (Moles et al. 1997) and now from NGC 7318b. The morphology of SQ galaxies reveals many signs of interaction including: (1) an apparently unrelaxed stellar halo comprising 30% of the optical light (Moles et al. 1998), (2) twin tidal tails of apparently different age (Sulentic et al. 2001) pointing toward the old intruder, (3) two spiral galaxies (NGC 7319 and old intruder) stripped of the bulk of their non-stellar material (Sulentic

et al. 2001). The IGM of SQ also reveals a complex debris field including hot ($\approx 10^6$ K, Trinchieri et al. 2005), warm ($\approx 10^4$ K, Xu et al. 1999; Sulentic et al. 2001) and cold – atomic ($\approx 10^2$ K, Williams et al. 2002) and molecular (≈ 10 –1000 K, Lisenfeld et al. 2004; Appleton et al. 2006) – gas. Also, recent star formation activity throughout a very extended disk shaped region around galaxies NGC 7318b and NGC 7318a has been reported from UV GALEX (Xu et al. 2005) and H α (Moles et al. 1997; Vílchez & Iglesias-Páramo 1998; Iglesias-Páramo & Vílchez 1999) images.

But perhaps the most conspicuous and interesting feature of SQ involves the close pair of galaxies NGC 7318a and NGC 7318b. Their recession velocities differ by almost 1000 km s⁻¹ (6630 and 5774 km s⁻¹ respectively). Four galaxies in SQ show radial velocities very close to the former value¹ implying that NGC 7318b is a new intruder entering the group from the far side and colliding with NGC 7318a, NGC 7319 and a complex debris field between them. The reality of this collision was confirmed by detection of an extended shock front in X-ray, optical and radio continuum light. The observational evidences suggest that NGC 7318b has passed through SQ after

[★] Based on observations taken at the 3.5m telescope at Calar Alto Observatory

¹ Hickson et al. (1992) proposed a value of $v = 6450$ km s⁻¹ as the recession velocity of the group.

entering from the far side with a high line-of-sight velocity. This large velocity difference argues that the bulk of its motion should be along the line of sight. All likely smaller transverse components of motion is indicated by the diffuse X-ray morphology: the West edge of the shock is somewhat sharper than the East (see e.g. E-W profile cuts in Trinchieri et al. 2005). We therefore assume that NGC 7318b has already passed through the group and is now in front of SQ.

The short crossing time of NGC 7318b² ($t_c \approx 1.2 \times 10^8$ yr) implies that we are seeing the collision *in flagrante delicto* or *post flagrantem delictum*. The latter possibility would mean that the intruder is seen projected on SQ.

Optical (long slit) spectroscopy of the shock-front has been reported in several papers (Ohyama et al. 1998; Xu et al. 2003). The latter authors identify at least three different emission components in this region but detailed study was restricted to the brightest regions. A complete mapping of physical and dynamical properties along the shock region is still lacking but has become feasible with Integral Field Unit (IFU) spectrographs. We present IFU observations at three positions in or near to the shock front. Our goal is to unravel the complex kinematics and excitation properties of the ionized gas along the path of the collision. The paper is organized as follows: Section 2 presents the instrumental setup and details about the observations and data reduction. A description of the data analysis and main results of the line fitting procedure are contained in Section 3. Section 4 presents discussion of the implications of our results and a summary of the main conclusions is presented in Section 5. Finally, Appendix A contains the details on the fitting procedure.

2. Data acquisition and reduction

SQ was observed on 2009 August 21-25 at Calar Alto Observatory (Almería, Spain), using the 3.5m Telescope with the Potsdam Multi-Aperture Spectrometer (PMAS, Roth et al. 2005). The standard lens array integral field unit (IFU) of $16'' \times 16''$ field of view (FOV) was used with a sampling of $1''$. The position of the IFU covering different regions of SQ – hereafter we will refer to them as pointings N, M and S – is shown in Figure 1. The figure also shows the position of the most remarkable H α structures reported in Williams et al. (2002).

Most of the optical range was covered with the R600 grating using two grating rotator angles: 143.3, covering from 3810 to 5394Å; and 146.05, covering from 5305 to 6809Å. The effective spectral resolution was 3.6Å FWHM (≈ 166 km s⁻¹ at H α). The blue and red spectra have a total integration time of 3600 seconds (split into three 1200 s individual dithered exposures), respectively, in fields N and S and 4200 seconds (split into three 1200 s and one 600 s dithered exposures) in the red one for the M field. Table 1 gives the coordinates, observation date, integration time, seeing conditions, as well as the median airmass during the observations and the overall photometric conditions during each observing night for the three pointings. Observations were taken under photometric conditions during the night of August 22, and under non photometric conditions during the rest of the nights.

² The crossing time of NGC 7318b was estimated as $t_c = D/\Delta v_{rad}$, where D is the diameter of the smallest circle containing the nuclei of all the galaxies (from Hickson et al. (1982), and Δv_{rad} is the difference in the radial velocities of SQ (6446 km s⁻¹, from NED) and NGC 7318b (7445 km s⁻¹, also from NED). The assumed distance for SQ is 88.6 Mpc (from NED).

The data were reduced following the standard steps for fiber-based integral field spectroscopy using the IRAF³ reduction package SPECRED. Bias was removed using a master-bias made out of combination of individual bias. Continuum lamps were taken before science exposure needed to identify the location of the 256 individual spectra on the CCD and extract them. We then performed a wavelength calibration using the HgNe lamp exposures taken before each science exposure. The continuum lamp and sky flats were used to determine the response of the instrument for each fiber and wavelength. Observations of the spectrophotometric standard stars BD +33°2642 and Cyg Ob2-9 were used for flux calibration co-adding the spectra of the central fibers and compared them with the tabulated one-dimensional spectra. The error of this calibration is of the order of 5%. The typical seeing during the observations was between 1.2'' and 1.5''.

The final products of our data reduction process are three 16×16 arrays each one composed of 256 spaxels containing the (blue and red) spectra of each pointing. However, given the low signal-to-noise ratio of the individual spectra we preferred to perform a 2×2 binning that improves the quality of the resulting spectra and possibilities a more detailed analysis. Figures 2 to 4 show the flux of all spaxels of each pointing along the spectral region $6650\text{Å} < \lambda < 6750\text{Å}$, which corresponds to the expected position of the [NII] $\lambda 6548, 6583\text{Å}$ and H α lines according to the typical recession velocities of the galaxies in SQ. At the end, each pointing corresponds to a 8×8 array, with spaxels of size $2'' \times 2''$. In what follows we will always refer to these binned spectra and we will work with the three 8×8 arrays corresponding to our three pointings. The spaxels will be named as $A[x,y]$, where A is one of the three pointings (S, M or N), x and y corresponds to the cartesian coordinates in the 8×8 array (as shown in figures 2 to 4), where [1,1] and [8,8] correspond to the Southeast and the Northwest corners respectively.

3. Results

A visual inspection of figures 2 to 4 reveals that in pointing S the flux is concentrated in few spaxels where the H α and [NII] lines are clearly visible. This situation is not the same in pointings M and N where the flux from emission lines is distributed in a more homogeneous way. Another interesting feature is that while the brightest spectra of pointing S show three narrow emission lines clearly resolved, unequivocally identified as the H α and [NII] $\lambda 6548, 6583\text{Å}$ lines, the spectra of pointings M and N show broader features severely blended. We notice that Xu et al. (2003) also found variable linewidths spanning the range 200 to 1000 km s⁻¹ in their long slit spectroscopic data of the shocked region. However, the non coincidence in the spatial position of the spectra and the different instrumental resolution prevents a detailed and quantitative comparison between both sets of data.

The physical properties of the ionized gas were estimated after individual fits to the most conspicuous emission lines of each spaxel. As the blue spectra are dominated by the background noise⁴, and the [SII] $\lambda 6717, 6731\text{Å}$ doublet did not fit in the our red spectral range, we use only the most intense lines of the

³ IRAF is distributed by the National Optical Astronomy Observatory, which is operated by the Association of Universities for Research in Astronomy (AURA) under cooperative agreement with the National Science Foundation.

⁴ Specially towards wavelengths bluewards 4500Å. In particular, the [OII] $\lambda 3727, 3729\text{Å}$ lines were not detected in any of the spectra.

red spectra for the fit: [O I] λ 6300Å, [N II] λ 6548,6583Å and H α . Details about the fitting procedure are explained in Appendix A.

The main results of the fit are shown in Tables 2 to 4. The recession velocities and integrated fluxes of each emission line are those resulting from the fit. The velocity dispersions have been estimated by assuming that the observed width of the line is the quadratic sum of different components (Richer et al. 2010):

$$\sigma^2 = \sigma_{obs}^2 - \sigma_{fs}^2 - \sigma_{ins}^2 - \sigma_{ther}^2 \quad (1)$$

where, σ_{obs} is the value obtained from the fit, σ_{fs} corresponds to the fine structure broadening and is taken equal to 3.199 km s^{-1} for H α (García Díaz et al. 2008), σ_{ins} corresponds to the instrumental broadening and is equal to 61.7 km s^{-1} , and σ_{ther} corresponds to the thermal broadening and is taken to be equal to 9.1 km s^{-1} assuming an electronic temperature of 10000 K (Osterbrock 1989). The spectra corresponding to the components S[7,5]b, S[7,7]a and N[6,1]a give negative values of σ^2 , probably due to small uncertainties in the determination of σ_{ins} . The uncertainty in the measured value of σ_{ins} is $\approx 5\%$, as determined from the widths of the arc lines. Thus, for these spectra giving negative values of σ^2 , we assumed a value of σ_{ins} equal to 0.95 the average value and computed an upper limit of $\sigma = 16.7 \text{ km s}^{-1}$.

As it is explained in the Appendix, we have performed a 2-component fit to all the spaxels in the three pointings. In order to avoid spurious results, only those components for which the intensity peak of the H α line is above $5 \times \Sigma_{bkg}$ are considered in this work. This means that after the fit, each spaxel can have associated 0, 1 or 2 components, depending on the corresponding signal to noise. For the rest of the lines, we measure the fluxes of those for which the intensity peak is above Σ_{bkg} , and give the corresponding upper limits otherwise. In what follows, we will refer to the low and high velocity components as A and B.

3.1. Properties of the emission lines

Figures 5 to 7 show some properties of the main emission lines of the three pointings based on the results issued of our fitting procedure. As it can be seen, the emission coming from pointing S is dominated by component A (where component B is almost absent), contrarily to what occurs in pointings M and N. The velocity of component A is constrained between 5500 and 6000 km s^{-1} in pointing S, it spans a range between 5800 and 6300 km s^{-1} in pointing M and it concentrates between 6000 and 6300 km s^{-1} in pointing N. On the contrary, component B ranges between 6500 and 6800 km s^{-1} in most spaxels of the three pointings. The velocity dispersions of component A are low and typical of those of H II regions ($20 \leq \sigma \leq 40 \text{ km s}^{-1}$) for the brightest spaxels of pointings S and M (S[2,2], S[2,3], S[5,2] and M[2,2]) but show larger values for fainter spaxels of pointings S and M, suggesting that the ionization source of these spectra is not dominated by recent star forming regions. In pointings M and N the velocity dispersion of most component A spaxels ranges between 100 and 200 km s^{-1} . Concerning component B, the velocity dispersions show values larger than 100 km s^{-1} for most spaxels. Finally, the [N II] λ 6583Å/H α ratio show values between 0.3 and 0.4 for the brightest spaxels in pointings S and M, which correspond to component A. Again, these values are consistent with the ones found for H II regions. The rest of the low velocity component spaxels, including those of pointing N, show values ≥ 0.4 in most cases. Conversely, spectra corresponding to component B tend to show values of the order or lower than 0.3 in the three pointings.

Figure 8 shows the H α intensity maps and radial velocity of components A and B for the three pointings⁵ and illustrate in a graphical way what we have previously stated. We remark the fact that component A increases its recession velocity as we move from pointing S to N, that is, from the southern edge to the core of the shock region.

Spaxels showing H II-like spectra (S[2,2], S[2,3], S[5,2] and M[2,2]) correspond with 3 H II regions clearly seen in the HST image. Optical spectra of these H II regions were previously obtained with the HET (Gallagher et al. 2001, their figure 14) and show recession velocities similar to the ones we find. These H II regions are associated with the Southern arm of NGC 7318b and either they have survived the shock or they passed through SQ without any interaction. Their oxygen abundances are shown in Table 5. They have been estimated following of Pettini & Pagel (2004) using the O3N2 indicator. Instead of a single value, the abundances show a gradient from the tip of the spiral arm (S[5,2], O/H \approx 58% the solar value) to the inner region (M[2,2], O/H \approx 83% the solar value). We assume the solar value is $12 + \log[\text{O}/\text{H}] = 8.69 \pm 0.05$ (Allende-Prieto et al. 2001).

3.2. Diagnostic diagrams

As we have seen in the previous subsection, many of our optical spectra show velocity dispersions and [N II]/H α ratios too large to be consistent with those of star forming regions. In fact, very few of them show clear signatures of being H II regions. There is also a non negligible fraction of spectra whose properties are not easily assignable to either of the two classes, because of a combination of broad emission lines and low [N II]/H α ratios.

For this reason we compare our data to two sets of theoretical models describing the properties of emission lines in star formation regions and shocks. Figures 9 to 11 show the [N II] λ 6583Å/H α vs. [O I] λ 6300Å/H α for the spectra of the three pointings. This diagnostic diagram has revealed to be suitable to disentangle the nature of the process responsible for the properties of the ionized gas at each spaxel. We have overplotted in the diagram two sets of models of ionized gas:

- Star formation models from Dopita et al. (2006): These models are parametrized by the metallicity of the ionizing stars and gas, the age of the stellar population and the parameter R , that accounts for the weak coupling between the ionization parameter and both the pressure of the ISM and the mass of the stellar cluster (see Dopita et al. 2006 for details). We have included in the plot models with solar and 0.4 solar metallicity, values of $R = 2, -2$ and -6 , along a time range between 0.1 and 6 Myr.
- Shock+precursor models from Allen et al. (2008): The complete library of models includes the radiative shock component as well as the photoionized precursor. In this work we selected only the models corresponding to solar and SMC metallicity, pre-shock density of 0.1, 1 and 10 cm^{-3} (only 1 cm^{-3} for the SMC models), and shock velocity values of $v_s = 100, 300$ and 1000 km s^{-1} , for a range of values of the magnetic field between 10^{-4} to 1000 μG .

The figures show that for solar metallicity the shock and star formation models are well separated from each other, overlapping only for the shock models with the lowest shock velocities (i.e. $v_s = 100 \text{ km s}^{-1}$ in this work). However, this does not hold when including lower metallicities. In particular,

⁵ The maps of component B corresponding to pointing S are not included since this component is almost undetected at this pointing.

the SMC shock models of low and intermediate shock velocity ($v_s \leq 300 \text{ km s}^{-1}$) overlap with the solar metallicity star formation models. This fact underlines the point that information on the metallicity (which is not available with the present data) is required in order to analyze the nature of emitting gas when shocks are likely to be present.

The first thing we notice is that, with the exception of the spaxels corresponding to the H α regions and some fainter spaxels of pointing S, the position of components A and B lay well above the H α regions from spiral and irregular galaxies from van Zee et al. (1998) and van Zee & Haynes (2006), supporting that the main source of ionization is shock rather than star formation. This result is also consistent with the conclusions of Cluver et al. (2010) from H $_2$ observations in the shocked region.

The brightest components of pointing S occupy the locus of the solar metallicity star formation models, whereas the fainter ones are located towards larger values of [O I]/H α , fairly consistent with the solar metallicity shock models with v_s increasing up to $\approx 300 \text{ km s}^{-1}$, or with the low metallicity (SMC) shock models with v_s between 300 and 1000 km s^{-1} . The velocity dispersions tend to be larger for those components closer to the shock models than to the star formation ones, although a strong relation is not observed. The position of pointing S with respect to the X-ray emission delineating the shock (e.g. Trinchieri et al. 2005), the radial velocities of most components and their velocity dispersions not very high as compared to those measured in pointings M and N, suggest that only a moderate fraction of the spaxels in pointing S could be affected by the shock induced by the collision of NGC 7318b with SQ. The rest of the spaxels of pointing S must correspond to the diffuse ionized medium present between the H α regions of normal spiral galaxies.

Concerning pointing M, the low velocity component of the bright spaxel M[2,2] is located between the solar metallicity star formation and shock models and it shows a low velocity dispersion, as it would be expected for an H α region. The rest of the components delineate a strip overlapping with the solar metallicity shock models ($100 \leq v_s \leq 300 \text{ km s}^{-1}$), and the SMC shock models ($300 \leq v_s \leq 1000 \text{ km s}^{-1}$). The velocity dispersions of most components are large and of the same order as expected for shock ionized spectra.

Finally, pointing N shows a very similar picture as pointing M, but without any spaxel showing an H α -like spectrum, most of the components showing properties of shock ionized spectra.

A remarkable point emerging from diagrams corresponding to pointings M and N is that component A spectra are preferentially located in the locus occupied by the solar metallicity shock models, whereas component B spectra are shifted towards the low metallicity (SMC) shock models. This suggests that the shock induced by the passage of NGC 7318b through SQ has involved at least two filaments of different recession velocities and metallicities.

4. Discussion

4.1. H α filaments and ionized gas components

The overall picture emerging from our observations can be summarized as follows: in most spaxels of our three pointings, two components are detected. A low velocity one (component A) – which shows H α -like spectra in a reduced number of spaxels of pointings S and M, and shock-like spectra in most spaxels of pointings M and N – and a high velocity one (component B) – which shows basically shock-like spectra in most spaxels of pointings M and N –. That is, the shock mostly affects pointings

M and N but not pointing S. The H α -like spectra correspond to star forming regions clearly seen in the HST optical images, what suggest that they passed through SQ with minimal disruption. This is consistent with what we see on the full resolution HST image of SQ and with a slit spectrum obtained with HET⁶ (Gallagher et al. 2001; figure 14) which partially overlaps with our pointing S.

Observations at other wavelengths show a link between different gaseous phases in the shock region: whereas the H α observations of Williams et al. (2002) show almost no gas along the ridge of the shock, H $_2$ was detected coincident with the ionized emission observed in our spectra (Appleton et al. 2006; Cluver et al. 2010). Despite the presence of dust signatures in this region (Guillard et al. 2010), no active star formation has been detected in the shock ridge, in agreement with the properties of the emission lines of the ionized gas.

An interesting point is that our observations show that the shock involves two filaments of (ionized) gas with recession velocities similar to the H α filaments reported by Williams et al. (2002). Together with the detection of H $_2$ gas in the ridge of the shock region, this suggests that the shock region was occupied by H α filaments that were converted into molecular and ionized gas respectively after the collision between NGC 7318b and SQ (Sulentic et al. 2001, Guillard et al. 2009).

One of these shocked ionized components shows a recession velocity between 6000 and 6300 km s^{-1} (component A in pointings M and N), which is in good agreement with the NW-LV H α cloud of Williams et al. (2002) to the North of the shocked region. The high velocity shocked ionized component shows a recession velocity of $\approx 6500 \text{ km s}^{-1}$ (component B in pointings M and N), which is consistent with those of the NW-HV, Arc-S and Arc-N H α filaments of Williams et al. (2002), and its emission line ratios are consistent with shock models of metallicities lower than solar (close to the value of the SMC).

The recent hydrodynamical simulations of Hwang et al. (2011) suggest that the gas dynamically associated to our two shocked ionized components comes mostly from NGC 7318b (although a small fraction also from NGC 7319) in the case of component A, and from NGC 7319 in the case of component B. Thus, we must address the point of whether these simulations are consistent with the information we have from the observations.

4.2. Metal abundances of the different components

Concerning component A, we know that the oxygen abundances of the H α regions detected in pointings S and M present a gradient where the oxygen abundance increases from pointing S towards pointing M. In particular, we estimated a value of 83% the solar value for the H α region detected in pointing M. As this region is located to the South of this pointing, we argue that the oxygen abundance of the shocked gas must be close to the solar value. Thus, if the gas at this velocity comes from the inner regions of NGC 7318b, as the hydrodynamical simulations suggest, the metallicity should be close to the solar value, according to our findings from the emission line properties of this component.

The case of component B is more complicated since we do not have direct information on the metallicity of the galaxy NGC 7319. For this reason, we look for indirect estimators of the metal content of the H α filaments dynamically associated to this

⁶ The HET spectrum includes three relatively normal H α regions in the new intruder followed by a velocity smeared region at $\sim 6050 \text{ km s}^{-1}$ and an uncertain detection at $\sim 6500 \text{ km s}^{-1}$.

component: Xu et al. (2003) performed long slit optical spectroscopy of a region (their spectrum M1) very close to NW-HV and to the infrared starburst SQ-A (Xu et al. 1999). Using the calibration of Kewley & Dopita (2002) they obtained a value of $12 + \log O/H = 8.76$ for values of $[NII]\lambda 6583\text{\AA}/H\alpha = 0.16$ and $[OIII]\lambda 5007\text{\AA}/H\beta = 2.48$. The estimations of the gas metallicity strongly depend on the calibration used, so a direct comparison between abundances estimated with different methods is not fair. When applying the calibration of Pettini & Pagel (2004) with the O3N2 indicator, we obtain $12 + \log O/H = 8.35$, which corresponds to 46% the solar value. Also, Lisenfeld et al. (2004) reported optical spectroscopic measurements of intergalactic star forming regions located in the tidal tails stemming from NGC 7319 and spatially coincident with the Arc-N filament, whose recession velocity is similar to that of Arc-S and NW-HV of Williams et al. (2002). These authors obtained $12 + \log O/H = 8.7$ using the calibration of van Zee et al. (1998), which implies a value of $[NII]\lambda 6583\text{\AA}/H\alpha \approx 0.24$ for the brightest region (SQ-B) at the tip of the tidal tail (P.-A. Duc, private communication). According to the calibration of Pettini & Pagel (2004), a lower value of $[NII]\lambda 6583\text{\AA}/H\alpha$ implies a lower value of the oxygen abundance. Comparing with the value measured for the HII region in S[5,2] ($[NII]\lambda 6583\text{\AA}/H\alpha \approx 0.30$) this means that the metallicity of SQ-B must be lower than 60% the solar value (which is the value estimated for S[5,2]). These two observational evidences together suggest that the high velocity gas filaments (NW-HV, Arc-S and Arc-N) must have metallicity significantly lower than solar, as the properties of the ionized component indicate.

But, is this result consistent with the suggestions of the simulations that the gas at this recession velocity comes from the galaxy NGC 7319? This question is relevant since other authors have suggested that the high velocity H I filaments could be the relics of the group formation process (Williams et al. 2002) instead of being tidal debris resulting from interactions among galaxies in the group (Moles et al. 1998). NGC 7319 is a high luminosity⁷ spiral galaxy that hosts an AGN in its nucleus. The fact that no H I was detected in the disk of this galaxy (Williams et al. 2002) supports the idea that this gas was removed from the disk in one of the interactions experienced by this galaxy and can now be found in the form of the neutral filaments seen around the main bodies of the galaxies. The metallicity of galaxies as luminous as NGC 7319 is difficult to estimate since it is well known the existence of gradients of abundances in spiral galaxies, so usually the external parts of the disk present lower abundances than the inner ones. Pilyugin et al. (2004) presented a study of oxygen gradients along a sample of spiral galaxies where they established a relation between the absolute magnitude of spirals and their characteristic metallicity, which is the metallicity measured at a distance from the center of $0.4R_{25}$. According to these authors, this average characteristic metallicity for a typical spiral as luminous as NGC 7319 is $12 + \log O/H \approx 8.6$. These authors also found that the oxygen abundance can reach levels as low as $12 + \log O/H = 8.2$ at distances from the galaxy nucleus between 0.5 and $0.9R_{25}$, even for galaxies as luminous as NGC 7319.

Putting all these arguments together, we have shown that the two ionized components detected in our bidimensional spectroscopic study of the shock region are kinematically consistent with the H I filaments and that their estimated metallicities are not inconsistent with the origin of these filaments, according to the results of the recent hydrodynamical simulations. The final picture of SQ emerging from our observations suggests the exist-

tence of a low velocity component showing normal HII emission at pointing S (where the recession velocity is consistent with that of NGC 7318b) and shocked emission in pointings M and N where the recession velocity is larger. In between the recession velocity this component shows a smooth gradient suggesting that this component was initially associated to the intruder galaxy NGC 7318b before the shock and that the northern part is currently shocked whereas the southern one has survived the shock probably because it has not encountered material in its path through SQ.

However, an overestimation of the role of overlap in our emission line decompositions cannot be completely discarded. Almost certainly there is SQ gas in the range $6600\text{--}6700 \text{ km s}^{-1}$ and new intruder gas from $5400\text{--}5800 \text{ km s}^{-1}$. Gas in the range $5800\text{--}6600 \text{ km s}^{-1}$ is the most difficult to interpret. The deep HST image suggest impressive destruction of structure (from spiral arms to HII regions) in the region of our pointings. As one example we could consider spaxel M[3,4] (not an extreme example, see Figure 18) where we think to see the signature of a new intruder HII region at $\approx 5900 \text{ km s}^{-1}$ with high $[NII]/H\alpha$. We model a second component with $v \approx 6400 \text{ km s}^{-1}$ with more typical $[NII]/H\alpha \approx 0.2$. This is not a unique solution and rather than a second component the strong red wing on the $H\alpha$ profile may be the signature of an emission tail due to ablation of the new intruder HII region. Data with higher signal-to-noise would make possible a more detailed consideration of shock related effects.

5. Summary and Conclusions

This work has presented a 3-D spectroscopic study of the ionized gas properties of three regions along the shocked bar-like structure in front of the pair of galaxies NGC 7318b and NGC 7318a. The analysis of the red part of the spectra around the $H\alpha$ line has revealed the existence of the following kinematical regimes:

- Spectra corresponding to 3 discrete emission features in pointings S and M: their recession velocities are consistent with that of NGC 7318b. The estimated oxygen abundances, $8.45 < 12 + \log O/H < 8.61$, are lower than the solar value and show a gradient along the spiral arm of NGC 7318b. We claim that these HII regions survived the collision of NGC 7318b with SQ.
- A low velocity shocked component, showing recession velocities in the range $5800 - 6300 \text{ km s}^{-1}$, and partially covering pointings S and M: its recession velocity increases in a smooth way as we move Northwards (from S to M) and the properties of this shocked ionized gas resemble those of solar metallicity shocked gas with velocity around 300 km s^{-1} . We propose that prior to the collision this ionized component was associated to the NW-LV H I filament of Williams et al. (2002).
- A high velocity shocked ionized component, present in the three pointings studied in this work although at a very low surface brightness in pointing S: this component shows a fairly constant recession velocity of $\approx 6600 \text{ km s}^{-1}$. Unlike the low velocity component, the properties of the high velocity component are consistent with those of a low metallicity shocked gas with velocity in the range $300 - 1000 \text{ km s}^{-1}$. This shocked ionized component is proposed to be the link between the NW-HV and Arc-S and Arc-N H I structures reported by Williams et al. (2002), and its oxygen abundance is consistent with being formed out of gas formerly in the disk of NGC 7319.

⁷ $M_B = -21.68$ according to LEDA.

The analysis presented in this work has shown the intriguing kinematical structure of this region, as it has been stated by the presence of blended components with different properties. Although some light has been shed in the relations between the ionized and neutral gaseous components detected around this region, their nature and origin is still far from being totally understood. For this reason, further observations with higher spatial and spectral resolution are needed to clarify in detail the state of the complex physical processes that are taking place in SQ.

Acknowledgements. We thank the anonymous referee for useful comments and suggestions that contributed to improve this paper. This work has been funded by the Spanish MICINN under the AYA2007-67965-C03-02 and the Consolider-Ingenio 2010 Program CSD2006-0070 “First Science with the GTC” grants. This research has made use of the NASA/IPAC Extragalactic Database (NED) which is operated by the Jet Propulsion Laboratory, California Institute of Technology, under contract with the National Aeronautics and Space Administration. We acknowledge the usage of the HyperLeda database (<http://leda.univ-lyon1.fr>)

References

- Allen, R. J., & Hartsuiker, J. W. 1972, *Nature*, 239, 324
- Allen, M. G., Groves, B. A., Dopita, M. A., Sutherland, R. S., & Kewley, L. J. 2008, *ApJS*, 178, 20
- Allende Prieto, C., Lambert, D. L., & Asplund, M. 2001, *ApJ*, 556, L63
- Appleton, P. N., et al. 2006, *ApJ*, 639, L51
- Arp, H. 1973, *ApJ*, 183, 411
- Athanassoula, E., Makino, J., & Bosma, A. 1997, *MNRAS*, 286, 825
- Athanassoula, E., Garijo, A., & García Gómez, C. 2001, *MNRAS*, 321, 353
- Awaki, H., Koyama, K., Matsumoto, H., Tomida, H., Tsuru, T., & Ueno, S. 1997, *PASJ*, 49, 445
- Burbidge, E. M., & Burbidge, G. R. 1961, *ApJ*, 134, 244
- Cluver, M. E., Appleton, P. N., Boulanger, F., et al. 2010, *ApJ*, 710, 248
- Dopita, M. A., & Sutherland, R. S. 1995, *ApJ*, 455, 468
- Dopita, M. A., et al. 2006, *ApJS*, 167, 177
- Gallagher, S. C., Charlton, J. C., Hunsberger, S. D., Zaritsky, D., & Whitmore, B. C. 2001, *AJ*, 122, 163
- García-Díaz, M. T., Henney, W. J., López, J. A., & Doi, T. 2008, *Rev. Mexicana Astron. Astrofis.*, 44, 181
- Guillard, P., Boulanger, F., Pineau Des Forêts, G., & Appleton, P. N. 2009, *A&A*, 502, 515
- Guillard, P., Boulanger, F., Cluver, M. E., et al. 2010, *A&A*, 518, A59
- Hickson, P. 1982, *ApJ*, 255, 382
- Hickson, P., Mendes de Oliveira, C., Huchra, J. P., & Palumbo, G. G. 1992, *ApJ*, 399, 353
- Hwang, J.-S., Struck, C., Renaud, F., & Appleton, P. 2011, arXiv:1109.4161
- Iglesias-Páramo, J., & Vílchez, J. M. 1999, *ApJ*, 518, 94
- Lisenfeld, U., Braine, J., Duc, P.-A., Brinks, E., Charmandaris, V., & Leon, S. 2004, *A&A*, 426, 471
- Markwardt, C. B. 2009, *Astronomical Society of the Pacific Conference Series*, 411, 251
- Mendes de Oliveira, C., Cypriano, E. S., Sodr e, L., Jr., & Balkowski, C. 2004, *ApJ*, 605, L17
- Miller, S. T., & Veilleux, S. 2003, *ApJ*, 592, 79
- Moles, M., Sulentic, J. W., & Marquez, I. 1997, *ApJ*, 485, L69
- Moles, M., Marquez, I., & Sulentic, J. W. 1998, *A&A*, 334, 473
- Ohyama, Y., Nishiura, S., Murayama, T., & Taniguchi, Y. 1998, *ApJ*, 492, L25
- Osterbrock, D. E. 1989, Research supported by the University of California, John Simon Guggenheim Memorial Foundation, University of Minnesota, et al. Mill Valley, CA, University Science Books, 1989, 422 p.,
- O’Sullivan, E., Giacintucci, S., Vrtilik, J. M., Raychaudhury, S., & David, L. P. 2009, *ApJ*, 701, 1560
- Pettini, M., & Pagel, B. E. J. 2004, *MNRAS*, 348, L59
- Pietsch, W., Trinchieri, G., Arp, H., & Sulentic, J. W. 1997, *A&A*, 322, 89
- Pilyugin, L. S., Vílchez, J. M., & Contini, T. 2004, *A&A*, 425, 849
- Plana, H., Mendes de Oliveira, C., Amram, P., Bolte, M., Balkowski, C., & Boulesteix, J. 1999, *ApJ*, 516, L69
- Relaño, M., Beckman, J. E., Zurita, A., Rozas, M., & Giammanco, C. 2005, *A&A*, 431, 235
- Richer, M. G., López, J. A., García-Díaz, M. T., Clark, D. M., Pereyra, M., & Díaz-Méndez, E. 2010, *ApJ*, 716, 857
- Roth, M. M., et al. 2005, *PASP*, 117, 620
- Saracco, P., & Ciliegi, P. 1995, *A&A*, 301, 348
- Shostak, G. S., Allen, R. J., & Sullivan, W. T., III 1984, *A&A*, 139, 15
- Stephan, M. E. 1877, *CR Acad. Sci. Paris*, 84, 641
- Sulentic, J. W., Pietsch, W., & Arp, H. 1995, *A&A*, 298, 420
- Sulentic, J. W., Rosado, M., Dultzin-Hacyan, D., Verdes-Montenegro, L., Trinchieri, G., Xu, C., & Pietsch, W. 2001, *AJ*, 122, 2993
- Trinchieri, G., Sulentic, J., Breitschwerdt, D., & Pietsch, W. 2003, *A&A*, 401, 173
- Trinchieri, G., Sulentic, J., Pietsch, W., & Breitschwerdt, D. 2005, *A&A*, 444, 697
- van der Hulst, J. M., & Rots, A. H. 1981, *AJ*, 86, 1775
- van Zee, L., Salzer, J. J., Haynes, M. P., O’Donoghue, A. A., & Balonek, T. J. 1998, *AJ*, 116, 2805
- van Zee, L., & Haynes, M. P. 2006, *ApJ*, 636, 214
- Verdes-Montenegro, L., Yun, M. S., Williams, B. A., Huchtmeier, W. K., Del Olmo, A., & Perea, J. 2001, *A&A*, 377, 812
- Vílchez, J. M., & Iglesias-Páramo, J. 1998, *ApJS*, 117, 1
- Williams, B. A., Yun, M. S., & Verdes-Montenegro, L. 2002, *AJ*, 123, 2417
- Xanthopoulos, E., Muxlow, T. W. B., Thomasson, P., & Garrington, S. T. 2004, *MNRAS*, 353, 1117
- Xu, C., Sulentic, J. W., & Tuffs, R. 1999, *ApJ*, 512, 178
- Xu, C. K., Lu, N., Condon, J. J., Dopita, M., & Tuffs, R. J. 2003, *ApJ*, 595, 665
- Xu, C. K., et al. 2005, *ApJ*, 619, L95
- Yun, M. S., Verdes-Montenegro, L., del Olmo, A., & Perea, J. 1997, *ApJ*, 475, L21

Appendix A: Details on the fitting procedure

The fitting procedure was performed as follows: for each pointing, we performed a 2×2 binning of all the spaxels in order to improve the signal to noise ratio of the resulting spectra. Then, for each spaxel, we fit the spectral range $[6620, 6780] \text{ \AA}$ to a set of gaussians corresponding to the emission lines $[\text{NII}]\lambda 6548, 6583 \text{ \AA}$ and $\text{H}\alpha$, under the following conditions:

- The intensities of the four emission lines must always be positive or zero (no underlying absorption in $\text{H}\alpha$ is assumed). In the case of $\text{H}\alpha$, we only allow intensity larger than zero.
- The recession velocity of the lines is restricted to the interval $[5400, 6900] \text{ km s}^{-1}$ (this seems reasonable since the recession velocities of all the galaxies of SQ are contained within this range).
- The theoretical relation $[\text{NII}]\lambda 6548/6583 = 0.333$ is preserved.
- The velocity dispersion (σ) of the three emission lines is forced to be the same, $> 1.35 \text{ \AA}$ (which is the nominal dispersion of the spectra), and $< 4.5 \text{ \AA}$. This last restriction is imposed to avoid non physical solutions that lead to arbitrarily broad lines for some spectra.

The continuum was estimated before the fit, it was assumed to be the same for the three emission lines and equal to the median flux in the spectral interval $[6600, 6660] \text{ \AA} \cup [6750, 6800] \text{ \AA}$. The background uncertainty (Σ_{bkg}) was taken to be equal to the standard deviation of the flux along this interval. After several tries, this was found to be a proper estimation given the almost null slope of the continuum along this spectral range. The fit was performed with the IDL based routine MPFITEXPR (Markwardt 2009). This code requires a set of initial input parameters ($I_{\text{H}\alpha}$, I_{6548} , v_{rec} and σ) and iteratively finds the solution that best matches the spectrum.

As mentioned in a previous section, figures 2 to 4 suggest the possibility that in some spaxels the emission comes from more than a single kinematical component. In order to decide the number of components we first try with a single component. Figure 12 shows the stacked spectra of the residuals after a 1-component fit for our three pointings. In the three cases the stacked residuals show an emission feature around 6710 \AA . This feature is broad for pointings S and M, and narrow and well defined in pointing N. The existence of these residual features could imply that we are missing a further component so we try again the fitting procedure with two components. Figure 13 shows stacked residuals after this 2-component fit and in this case we do not see any emission feature, the result being reasonably flat. For this reason, we decide to fix the number of kinematical components in two. Figures 14 to 16 show the residuals in the $[6650, 6750] \text{ \AA}$ spectral interval, after the subtraction of the 2-component $\text{H}\alpha + [\text{NII}]$ fitting. The residuals are quite flat, implying that our choice is reasonable.

Once the fit of these three lines is finished, we fit the $[\text{OI}]\lambda 6300 \text{ \AA}$ line in the red spectra and the $[\text{OIII}]\lambda 4959, 5007 \text{ \AA}$ and $\text{H}\beta$ lines in the blue spectra to gaussians with the redshifts and velocity dispersions resulting from the fit to the corresponding red spectra.

To illustrate the quality of the fits, we show in figures 17 to 19 three examples of typical fits of each pointing. Spaxel S[2,2] was fit to a single component and corresponds to one of the HII regions and shows a typical HII -like spectrum. Spaxels M[3,4] and N[4,4] were fit to two components and correspond to the shocked region. The red spectra show broad lines unlike the blue

spectra where few emission lines were detected. Figure 17 shows a conspicuous asymmetric residual at $\approx 6685 \text{ \AA}$, coincident with the strong $\text{H}\alpha$ line detected in spaxel S[2,2]. This residual is unexplained and since we do not see it for other bright $\text{H}\alpha$ lines or arcs, it is unlikely be due to an instrumental effect.

In order to avoid spurious results due to low signal-to-noise, throughout this paper we will keep only those components for which the intensity peak of the $\text{H}\alpha$ line is above $5 \times \Sigma_{bkg}$. This means that the maximum number of components detected for individual spaxels is 2, but could be 1 or even zero depending on the signal-to-noise of the $\text{H}\alpha$ line. For the rest of the lines, we fit a gaussian with σ and redshift equal to those of the corresponding $\text{H}\alpha$ line, and we measure the fluxes of all the lines for which the intensity peak is above $1 \times \Sigma_{bkg}$.

Please give a shorter version with: \authorrunning and/or \titilerunning prior to \maketitle

Pointing	R.A. (J2000.0)	Dec. (J2000.0)	Date	Exp. time (s)	Seeing (")	Airmass	Conditions [†]
S	22 35 59.0	33 57 38.0	Aug 24	3 × 1200	1.5	1.11	NP
M	22 35 59.5	33 57 55.0	Aug 25	3 × 1200	1.5	1.01	NP
N	22 36 00.0	33 58 10.0	Aug 22	3 × 1200	1.2	1.12	P

Table 1. Diary of the observations. [†] P (NP) stands for photometric (non photometric) atmospheric conditions.

Spaxel	v_{rad}	σ	$\Sigma_{bkg,blue}$	$f(H\beta)$	$f([OIII]\lambda 5007\text{\AA})$ $/f(H\beta)$	$\Sigma_{bkg,red}$	$f([OI]\lambda 6300\text{\AA})$ $/f(H\alpha)$	$f(H\alpha)$	$f([NII]\lambda 6583\text{\AA})$ $/f(H\alpha)$
S[1, 1]a	6607.5	70.4	1.38e-17	< 2.44e-15	—	6.02e-18	< 0.13	9.54e-15	0.15
S[1, 2]a	5704.8	90.4	1.70e-17	< 3.86e-15	—	5.51e-18	0.11	1.65e-14	0.08
S[1, 2]b	6615.0	171.9	1.70e-17	< 7.34e-15	—	5.51e-18	< 0.11	2.58e-14	0.09
S[1, 3]a	5728.5	109.2	1.95e-17	< 5.33e-15	—	5.68e-18	0.11	2.52e-14	0.48
S[1, 4]a	5934.0	181.2	1.67e-17	< 7.59e-15	—	6.03e-18	0.30	1.99e-14	0.40
S[1, 5]	—	—	—	—	—	—	—	—	—
S[1, 6]	—	—	—	—	—	—	—	—	—
S[1, 7]	—	—	—	—	—	—	—	—	—
S[1, 8]	—	—	—	—	—	—	—	—	—
S[2, 1]a	5725.5	52.1	1.47e-17	< 1.92e-15	—	5.45e-18	< 0.17	4.26e-15	0.63
S[2, 2]a	5670.9	38.7	1.28e-17	2.03e-14	1.94	4.46e-18	0.02	1.22e-13	0.32
S[2, 3]a	5676.9	41.0	1.88e-17	1.20e-14	1.76	5.35e-18	0.02	7.64e-14	0.36
S[2, 4]a	5809.8	98.3	1.50e-17	< 3.71e-15	—	5.02e-18	0.24	1.38e-14	0.14
S[2, 4]b	6730.2	196.0	1.50e-17	9.96e-15	< 1.59	5.02e-18	< 0.21	1.37e-14	< 0.18
S[2, 5]a	5942.4	145.6	1.37e-17	< 4.99e-15	—	5.74e-18	0.24	1.88e-14	0.11
S[2, 5]b	6872.4	130.7	1.37e-17	< 4.48e-15	—	5.74e-18	< 0.20	1.16e-14	0.16
S[2, 6]a	5964.0	165.9	1.68e-17	< 6.99e-15	—	5.03e-18	0.28	1.77e-14	< 0.12
S[2, 7]	—	—	—	—	—	—	—	—	—
S[2, 8]	—	—	—	—	—	—	—	—	—
S[3, 1]a	5744.1	102.2	1.37e-17	< 3.51e-15	—	4.69e-18	< 0.12	9.65e-15	0.64
S[3, 2]a	5730.6	78.6	1.29e-17	8.82e-15	1.30	5.15e-18	0.08	4.55e-14	0.45
S[3, 3]a	5742.3	79.5	1.41e-17	8.75e-15	1.45	5.33e-18	0.04	4.55e-14	0.50
S[3, 4]a	5800.8	72.9	1.11e-17	< 2.02e-15	—	4.95e-18	0.15	1.80e-14	0.39
S[3, 5]a	5876.1	101.2	1.53e-17	< 3.89e-15	—	5.63e-18	< 0.17	1.18e-14	< 0.12
S[3, 6]	—	—	—	—	—	—	—	—	—
S[3, 7]	—	—	—	—	—	—	—	—	—
S[3, 8]	—	—	—	—	—	—	—	—	—
S[4, 1]	—	—	—	—	—	—	—	—	—
S[4, 2]a	5777.1	93.1	1.34e-17	< 3.13e-15	—	4.67e-18	0.11	2.47e-14	0.37
S[4, 2]b	6603.6	38.4	1.34e-17	< 1.29e-15	—	4.67e-18	< 0.18	2.41e-15	< 0.19
S[4, 3]a	5732.4	78.0	1.66e-17	4.50e-15	1.68	4.69e-18	0.05	3.77e-14	0.43
S[4, 4]a	5780.7	113.0	1.37e-17	< 3.88e-15	—	5.45e-18	0.23	1.26e-14	0.38
S[4, 5]a	5796.3	102.9	1.39e-17	< 3.58e-15	—	5.23e-18	< 0.18	7.72e-15	0.67
S[4, 6]a	5809.2	117.2	1.52e-17	< 4.47e-15	—	4.63e-18	< 0.23	7.05e-15	0.25
S[4, 7]	—	—	—	—	—	—	—	—	—
S[4, 8]a	5817.0	81.2	1.46e-17	< 2.96e-15	—	4.76e-18	0.35	4.96e-15	0.83

Table 2. Properties of the emission lines for the spaxels of pointing S: (1) Spectrum Id. and component; (2) Recession velocity (km s⁻¹); (3) Velocity dispersion at $\lambda = 6563\text{\AA}$ (km s⁻¹); (4) Standard deviation of the background in the blue spectrum (erg s⁻¹ cm⁻² Å⁻¹); (5) Integrated flux of the H β line (erg s⁻¹ cm⁻²); (6) [OIII] $\lambda 5007$ /H β line flux ratio; (7) Standard deviation of the background in the red spectrum (erg s⁻¹ cm⁻² Å⁻¹); (8) [OI] $\lambda 6300$ /H α line flux ratio; (9) Integrated flux of the H α line (erg s⁻¹ cm⁻²); (10) [NII] $\lambda 6583$ /H α line flux ratio. Colons before numbers mean that the line intensity peaks are lower than 3 times the standard deviation of the corresponding background.

Please give a shorter version with: \authorrunning and/or \titilerunning prior to \maketitle

Spaxel	v_{rad}	σ	$\Sigma_{bkg,blue}$	$f(H\beta)$	$f([OIII]\lambda 5007\text{\AA})$ $/f(H\beta)$	$\Sigma_{bkg,red}$	$f([OI]\lambda 6300\text{\AA})$ $/f(H\alpha)$	$f(H\alpha)$	$f([NII]\lambda 6583\text{\AA})$ $/f(H\alpha)$
S[5, 1]a	5700.6	89.3	1.31e-17	5.18e-15	< 1.48	5.29e-18	< 0.13	9.04e-15	< 0.13
S[5, 2]a	5639.7	38.3	1.40e-17	1.48e-14	2.05	5.55e-18	0.02	1.21e-13	0.30
S[5, 3]a	5652.3	39.7	1.39e-17	8.90e-15	1.40	4.95e-18	0.05	3.94e-14	0.41
S[5, 4]	—	—	—	—	—	—	—	—	—
S[5, 5]	—	—	—	—	—	—	—	—	—
S[5, 6]a	5704.2	92.1	1.78e-17	< 4.12e-15	—	6.43e-18	< 0.23	8.96e-15	0.90
S[5, 7]a	5646.6	70.1	1.82e-17	< 3.19e-15	—	6.17e-18	< 0.07	2.35e-14	0.63
S[5, 8]a	5640.3	31.7	3.77e-17	< 3.00e-15	—	1.84e-17	< 0.20	7.87e-15	< 0.19
S[6, 1]a	5653.2	56.1	1.43e-17	< 2.01e-15	—	4.67e-18	0.15	1.06e-14	0.54
S[6, 2]a	5647.8	60.7	1.30e-17	9.13e-15	2.16	5.10e-18	0.07	3.82e-14	0.41
S[6, 3]a	5656.2	58.0	1.55e-17	3.42e-15	2.93	5.13e-18	< 0.05	1.83e-14	0.41
S[6, 4]	—	—	—	—	—	—	—	—	—
S[6, 5]a	6592.2	16.3	1.71e-17	< 6.99e-16	—	6.09e-18	< 0.16	1.59e-15	0.34
S[6, 6]a	5635.8	57.2	1.77e-17	< 2.54e-15	—	7.19e-18	0.25	8.79e-15	0.22
S[6, 7]a	5628.9	53.7	1.62e-17	5.58e-15	< 1.02	7.43e-18	< 0.05	2.20e-14	0.60
S[6, 8]a	5644.8	38.9	1.49e-17	< 1.45e-15	—	5.93e-18	0.19	7.77e-15	0.35
S[7, 1]a	5636.7	50.3	1.19e-17	5.65e-15	1.27	6.02e-18	0.04	4.69e-14	0.40
S[7, 2]a	5663.1	39.9	1.87e-17	< 1.88e-15	—	5.88e-18	0.08	1.05e-14	0.55
S[7, 3]	—	—	—	—	—	—	—	—	—
S[7, 4]	—	—	—	—	—	—	—	—	—
S[7, 5]a	5702.1	103.5	1.80e-17	< 4.67e-15	—	6.56e-18	0.35	1.07e-14	0.27
S[7, 5]b	6583.8	< 16.7	1.80e-17	< -7.53e-16	—	6.56e-18	< 0.23	-1.98e-15	< 0.14
S[7, 6]a	5654.4	40.7	2.01e-17	< 2.05e-15	—	7.57e-18	< 0.22	5.20e-15	0.59
S[7, 7]a	5673.9	< 16.7	2.14e-17	-1.98e-15	< 0.95	8.09e-18	0.27	-2.99e-15	0.79
S[7, 8]	—	—	—	—	—	—	—	—	—
S[8, 1]a	5626.2	31.2	1.71e-17	< 1.34e-15	—	5.70e-18	0.13	1.32e-14	0.39
S[8, 2]	—	—	—	—	—	—	—	—	—
S[8, 3]	—	—	—	—	—	—	—	—	—
S[8, 4]	—	—	—	—	—	—	—	—	—
S[8, 5]	—	—	—	—	—	—	—	—	—
S[8, 6]a	5654.7	65.7	1.71e-17	< 2.81e-15	—	7.06e-18	< 0.14	8.22e-15	0.88
S[8, 7]	—	—	—	—	—	—	—	—	—
S[8, 8]	—	—	—	—	—	—	—	—	—

Table 2. Continued.

Please give a shorter version with: \authorrunning and/or \titilerunning prior to \maketitle

Spaxel	v_{rad}	σ	$\Sigma_{bkg,blue}$	$f(H\beta)$	$f([OIII]\lambda 5007\text{\AA})$ $/f(H\beta)$	$\Sigma_{bkg,red}$	$f([OI]\lambda 6300\text{\AA})$ $/f(H\alpha)$	$f(H\alpha)$	$f([NII]\lambda 6583\text{\AA})$ $/f(H\alpha)$
M[1, 1]a	5836.8	63.3	1.66e-17	< 2.63e-15	—	3.81e-18	0.34	6.53e-15	0.61
M[1, 2]a	5812.8	64.2	1.59e-17	< 2.55e-15	—	4.83e-18	0.25	1.06e-14	0.62
M[1, 2]b	6207.6	196.0	1.59e-17	< 7.79e-15	—	4.83e-18	< 0.22	1.25e-14	0.24
M[1, 3]a	5832.3	50.0	1.62e-17	< 2.03e-15	—	4.54e-18	0.11	1.20e-14	0.48
M[1, 4]a	5814.3	14.8	1.61e-17	< 5.94e-16	—	5.14e-18	0.24	1.89e-15	0.34
M[1, 5]a	5810.7	55.3	2.14e-17	< 2.97e-15	—	7.11e-18	0.09	1.66e-14	0.52
M[1, 6]a	5922.0	112.3	1.50e-17	< 4.23e-15	—	4.84e-18	0.29	1.19e-14	0.32
M[1, 7]a	5955.9	112.4	2.74e-17	< 7.72e-15	—	5.02e-18	0.38	1.33e-14	0.28
M[1, 8]a	5916.3	63.9	4.24e-17	< 6.78e-15	—	1.54e-17	< 0.20	1.36e-14	0.19
M[2, 1]a	5827.5	78.9	1.21e-17	3.99e-15	< 1.67	3.44e-18	< 0.09	9.50e-15	0.09
M[2, 1]b	6789.9	166.7	1.21e-17	< 5.05e-15	—	3.44e-18	< 0.17	1.09e-14	0.13
M[2, 2]a	5772.3	22.6	1.42e-17	2.10e-15	1.01	3.38e-18	0.08	2.27e-14	0.42
M[2, 3]a	5814.0	53.2	1.62e-17	3.19e-15	< 1.48	4.89e-18	0.17	8.21e-15	0.91
M[2, 4]a	5952.6	142.5	1.25e-17	< 4.45e-15	—	4.13e-18	< 0.20	9.39e-15	0.43
M[2, 5]a	5974.8	128.2	1.25e-17	4.85e-15	< 2.05	4.48e-18	0.11	1.92e-14	0.67
M[2, 6]a	5952.0	123.2	1.56e-17	< 4.81e-15	—	4.66e-18	< 0.11	1.75e-14	0.61
M[2, 7]a	6004.8	134.5	1.45e-17	< 4.89e-15	—	4.66e-18	0.26	2.52e-14	0.54
M[2, 7]b	6655.8	196.0	1.45e-17	< 7.13e-15	—	4.66e-18	< 0.19	1.43e-14	0.28
M[2, 8]a	5977.5	100.4	1.71e-17	5.02e-15	< 1.65	5.48e-18	0.22	2.15e-14	0.68
M[2, 8]b	6644.4	196.0	1.71e-17	< 8.39e-15	—	5.48e-18	< 0.12	2.00e-14	0.23
M[3, 1]a	5912.1	108.4	1.36e-17	< 3.70e-15	—	3.99e-18	0.29	1.29e-14	0.48
M[3, 2]a	5839.8	86.7	1.43e-17	< 3.11e-15	—	3.74e-18	0.19	2.23e-14	0.72
M[3, 3]a	5880.0	78.2	1.26e-17	< 2.47e-15	—	4.91e-18	0.32	1.93e-14	0.70
M[3, 3]b	6329.4	196.0	1.26e-17	< 6.19e-15	—	4.91e-18	0.17	2.74e-14	0.22
M[3, 4]a	5918.1	109.5	1.76e-17	< 4.84e-15	—	4.78e-18	0.12	2.55e-14	0.94
M[3, 4]b	6349.8	196.0	1.76e-17	< 8.67e-15	—	4.78e-18	0.11	2.78e-14	0.24
M[3, 5]a	6058.2	159.7	1.70e-17	< 6.82e-15	—	4.21e-18	0.26	4.11e-14	0.59
M[3, 5]b	6692.1	196.0	1.70e-17	< 8.37e-15	—	4.21e-18	0.17	2.69e-14	0.36
M[3, 6]a	6099.3	183.9	1.39e-17	< 6.39e-15	—	3.98e-18	0.24	3.84e-14	0.68
M[3, 6]b	6677.1	160.6	1.39e-17	< 5.58e-15	—	3.98e-18	0.19	2.86e-14	0.24
M[3, 7]a	6058.5	155.7	1.51e-17	< 5.88e-15	—	5.05e-18	0.26	3.23e-14	0.54
M[3, 7]b	6663.3	170.6	1.51e-17	< 6.44e-15	—	5.05e-18	0.18	2.94e-14	0.22
M[3, 8]a	6040.8	144.0	1.50e-17	< 5.43e-15	—	5.21e-18	0.19	3.64e-14	0.54
M[3, 8]b	6671.1	180.6	1.50e-17	< 6.80e-15	—	5.21e-18	0.14	2.51e-14	0.22
M[4, 1]a	5965.5	137.4	1.36e-17	< 4.68e-15	—	4.02e-18	0.25	1.61e-14	0.35
M[4, 1]b	6849.6	142.8	1.36e-17	< 4.86e-15	—	4.02e-18	< 0.21	7.32e-15	< 0.20
M[4, 2]a	6040.2	157.1	1.41e-17	< 5.57e-15	—	4.37e-18	0.27	1.83e-14	0.57
M[4, 2]b	6688.8	196.0	1.41e-17	< 6.94e-15	—	4.37e-18	< 0.17	1.39e-14	< 0.15
M[4, 3]a	5985.6	77.7	1.45e-17	< 2.82e-15	—	3.97e-18	< 0.13	8.78e-15	0.54
M[4, 3]b	6527.1	196.0	1.45e-17	< 7.11e-15	—	3.97e-18	0.15	3.11e-14	0.21
M[4, 4]a	5981.4	120.8	1.18e-17	< 3.56e-15	—	4.24e-18	0.30	1.73e-14	0.63
M[4, 4]b	6555.3	196.0	1.18e-17	9.51e-15	< 1.54	4.24e-18	0.16	2.91e-14	0.23
M[4, 5]a	5986.8	120.6	1.41e-17	< 4.25e-15	—	3.86e-18	< 0.19	9.65e-15	0.69
M[4, 5]b	6702.0	168.1	1.41e-17	< 5.92e-15	—	3.86e-18	< 0.15	1.71e-14	0.10
M[4, 6]a	6093.6	161.4	1.61e-17	< 6.51e-15	—	3.46e-18	0.19	1.16e-14	0.60
M[4, 6]b	6715.5	150.6	1.61e-17	< 6.07e-15	—	3.46e-18	< 0.10	1.86e-14	0.27
M[4, 7]a	6051.0	118.7	1.26e-17	< 3.76e-15	—	4.70e-18	0.25	1.95e-14	0.66
M[4, 7]b	6650.1	196.0	1.26e-17	< 6.20e-15	—	4.70e-18	0.17	4.06e-14	0.26
M[4, 8]a	6021.6	98.2	1.39e-17	< 3.43e-15	—	4.09e-18	0.17	2.30e-14	0.71
M[4, 8]b	6568.2	196.0	1.39e-17	< 6.85e-15	—	4.09e-18	< 0.10	2.92e-14	0.26

Table 3. Same as Table 2 for the spaxels of pointing M.

Please give a shorter version with: \authorrunning and/or \titilerunning prior to \maketitle

Spaxel	v_{rad}	σ	$\Sigma_{bkg,blue}$	$f(H\beta)$	$f([OIII]\lambda 5007\text{\AA})$ $/f(H\beta)$	$\Sigma_{bkg,red}$	$f([OI]\lambda 6300\text{\AA})$ $/f(H\alpha)$	$f(H\alpha)$	$f([NII]\lambda 6583\text{\AA})$ $/f(H\alpha)$
M[5, 1]a	6073.5	169.1	1.37e-17	< 5.80e-15	—	4.42e-18	0.17	1.53e-14	0.38
M[5, 1]b	6658.2	148.1	1.37e-17	< 5.08e-15	—	4.42e-18	0.12	2.32e-14	0.15
M[5, 2]a	6135.3	88.8	1.35e-17	< 3.01e-15	—	4.72e-18	0.33	6.09e-15	< 0.17
M[5, 2]b	6736.2	132.6	1.35e-17	< 4.49e-15	—	4.72e-18	0.20	2.86e-14	0.21
M[5, 3]a	6663.0	167.4	1.66e-17	< 6.98e-15	—	4.56e-18	< 0.14	1.92e-14	0.20
M[5, 4]a	6701.4	120.5	1.56e-17	< 4.72e-15	—	5.19e-18	0.14	1.96e-14	0.29
M[5, 5]a	6130.2	92.9	2.04e-17	< 4.74e-15	—	5.48e-18	< 0.18	9.82e-15	0.55
M[5, 5]b	6663.3	131.0	2.04e-17	< 6.69e-15	—	5.48e-18	< 0.10	2.53e-14	0.13
M[5, 6]a	6148.2	28.1	1.60e-17	< 1.13e-15	—	5.06e-18	< 0.12	4.63e-15	0.64
M[5, 6]b	6691.8	139.7	1.60e-17	< 5.62e-15	—	5.06e-18	< 0.10	2.88e-14	0.25
M[5, 7]a	6206.4	122.7	1.69e-17	< 5.20e-15	—	5.11e-18	< 0.11	1.97e-14	0.56
M[5, 7]b	6718.5	196.0	1.69e-17	1.35e-14	< 1.89	5.11e-18	< 0.13	2.86e-14	0.23
M[5, 8]a	6255.0	123.7	4.79e-17	< 1.48e-14	—	1.58e-17	< 0.14	2.51e-14	0.41
M[6, 1]a	6682.2	108.7	1.62e-17	< 4.41e-15	—	4.17e-18	0.09	1.65e-14	0.24
M[6, 2]a	6712.5	141.5	1.46e-17	< 5.18e-15	—	4.08e-18	< 0.10	1.68e-14	< 0.09
M[6, 3]a	6729.9	142.8	1.41e-17	< 5.06e-15	—	4.40e-18	< 0.09	2.49e-14	0.24
M[6, 4]a	6626.1	181.5	1.57e-17	< 7.12e-15	—	3.74e-18	< 0.13	2.57e-14	0.29
M[6, 5]a	6702.3	196.0	1.50e-17	< 7.36e-15	—	5.05e-18	< 0.14	2.59e-14	0.13
M[6, 6]a	6236.7	85.7	1.64e-17	3.93e-15	< 2.05	4.66e-18	< 0.18	1.01e-14	0.50
M[6, 6]b	6723.6	196.0	1.64e-17	< 8.03e-15	—	4.66e-18	0.17	3.44e-14	0.16
M[6, 7]a	6221.1	124.4	1.66e-17	< 5.19e-15	—	4.54e-18	0.16	2.78e-14	0.52
M[6, 7]b	6670.2	196.0	1.66e-17	< 8.17e-15	—	4.54e-18	< 0.08	3.57e-14	0.22
M[6, 8]a	6078.9	87.5	1.55e-17	< 3.39e-15	—	5.28e-18	< 0.14	1.17e-14	0.88
M[6, 8]b	6458.4	196.0	1.55e-17	< 7.60e-15	—	5.28e-18	< 0.12	3.07e-14	0.26
M[7, 1]a	6733.5	82.0	1.56e-17	< 3.21e-15	—	4.91e-18	< 0.11	1.27e-14	0.15
M[7, 2]a	6726.6	117.5	1.95e-17	7.58e-15	< 1.46	5.47e-18	< 0.10	2.09e-14	0.19
M[7, 3]a	6701.1	98.0	2.10e-17	< 5.16e-15	—	6.18e-18	0.17	2.64e-14	0.30
M[7, 4]a	6660.6	134.8	2.26e-17	< 7.65e-15	—	5.12e-18	< 0.10	2.71e-14	0.21
M[7, 5]a	6234.6	132.0	1.81e-17	< 6.00e-15	—	5.17e-18	< 0.26	1.14e-14	0.21
M[7, 5]b	6696.6	196.0	1.81e-17	< 8.92e-15	—	5.17e-18	< 0.14	3.18e-14	< 0.08
M[7, 6]a	6670.2	196.0	2.12e-17	< 1.04e-14	—	6.81e-18	< 0.10	3.55e-14	0.20
M[7, 7]a	6475.5	196.0	2.15e-17	< 1.06e-14	—	7.09e-18	0.15	4.62e-14	0.17
M[7, 8]a	6399.9	170.4	2.14e-17	< 9.13e-15	—	7.97e-18	< 0.11	3.64e-14	0.32
M[8, 1]	—	—	—	—	—	—	—	—	—
M[8, 2]a	6633.0	170.0	2.05e-17	< 8.72e-15	—	5.32e-18	< 0.25	1.15e-14	< 0.20
M[8, 3]a	6077.7	73.2	1.95e-17	< 3.58e-15	—	5.10e-18	< 0.22	5.87e-15	0.35
M[8, 3]b	6682.5	196.0	1.95e-17	< 9.58e-15	—	5.10e-18	< 0.22	1.58e-14	< 0.16
M[8, 4]a	6175.2	98.9	1.80e-17	< 4.46e-15	—	6.43e-18	< 0.26	8.02e-15	0.65
M[8, 5]a	6540.9	196.0	1.93e-17	< 9.47e-15	—	5.85e-18	< 0.28	1.48e-14	0.19
M[8, 6]a	6603.3	196.0	1.80e-17	< 8.85e-15	—	4.73e-18	< 0.18	2.27e-14	0.23
M[8, 7]a	5828.7	32.8	1.69e-17	< 1.39e-15	—	5.77e-18	< 0.07	1.09e-14	0.14
M[8, 7]b	6540.9	196.0	1.69e-17	< 8.31e-15	—	5.77e-18	< 0.12	4.07e-14	0.26
M[8, 8]a	6399.9	196.0	2.24e-17	< 1.10e-14	—	8.50e-18	0.11	3.88e-14	< 0.11
M[8, 8]b	6465.3	19.3	2.24e-17	2.70e-15	< 0.79	8.50e-18	0.37	2.57e-15	1.08

Table 3. Continued.

Spaxel	v_{rad}	σ	$\Sigma_{bkg,blue}$	$f(H\beta)$	$f([OIII]\lambda 5007\text{\AA})$ $/f(H\beta)$	$\Sigma_{bkg,red}$	$f([OI]\lambda 6300\text{\AA})$ $/f(H\alpha)$	$f(H\alpha)$	$f([NII]\lambda 6583\text{\AA})$ $/f(H\alpha)$
N[1, 1]a	6061.2	157.3	1.68e-17	< 6.62e-15	—	3.90e-18	0.29	2.91e-14	0.64
N[1, 1]b	6660.9	175.0	1.68e-17	< 7.36e-15	—	3.90e-18	0.13	2.57e-14	0.25
N[1, 2]a	6061.2	146.0	1.45e-17	< 5.31e-15	—	3.98e-18	0.20	3.55e-14	0.62
N[1, 2]b	6627.0	112.2	1.45e-17	< 4.08e-15	—	3.98e-18	0.18	1.58e-14	0.24
N[1, 3]a	6148.8	173.9	1.43e-17	< 6.22e-15	—	5.33e-18	0.20	5.87e-14	0.58
N[1, 3]b	6651.0	160.9	1.43e-17	9.78e-15	< 1.25	5.33e-18	0.13	3.74e-14	0.22
N[1, 4]a	6115.8	148.9	1.40e-17	< 5.23e-15	—	3.87e-18	0.27	1.84e-14	0.67
N[1, 4]b	6661.2	157.4	1.40e-17	< 5.53e-15	—	3.87e-18	0.17	1.13e-14	< 0.13
N[1, 5]a	6102.6	134.1	1.93e-17	< 6.47e-15	—	6.47e-18	0.34	1.36e-14	0.92
N[1, 5]b	6578.1	179.8	1.93e-17	< 8.68e-15	—	6.47e-18	0.18	1.91e-14	0.33
N[1, 6]a	6093.6	135.2	1.55e-17	< 5.24e-15	—	4.01e-18	0.20	2.20e-14	0.73
N[1, 6]b	6563.4	153.9	1.55e-17	< 5.96e-15	—	4.01e-18	0.17	1.28e-14	0.48
N[1, 7]a	6114.0	148.2	1.99e-17	8.95e-15	< 1.91	4.84e-18	< 0.18	1.21e-14	0.64
N[1, 8]	—	—	—	—	—	—	—	—	—
N[2, 1]a	6075.6	154.8	1.29e-17	< 5.02e-15	—	4.18e-18	0.10	2.58e-14	0.79
N[2, 1]b	6661.8	159.9	1.29e-17	< 5.19e-15	—	4.18e-18	0.13	3.35e-14	0.26
N[2, 2]a	6036.6	121.3	1.34e-17	< 4.07e-15	—	4.27e-18	0.15	2.74e-14	0.78
N[2, 2]b	6575.1	196.0	1.34e-17	< 6.58e-15	—	4.27e-18	0.14	3.24e-14	0.25
N[2, 3]a	6099.0	151.0	1.30e-17	< 4.91e-15	—	4.41e-18	0.24	1.93e-14	0.74
N[2, 3]b	6676.8	196.0	1.30e-17	< 6.37e-15	—	4.41e-18	0.25	2.22e-14	0.24
N[2, 4]a	6165.6	163.4	1.33e-17	< 5.44e-15	—	3.89e-18	0.13	2.31e-14	0.45
N[2, 4]b	6742.8	150.8	1.33e-17	< 5.02e-15	—	3.89e-18	0.14	2.25e-14	0.17
N[2, 5]a	6077.7	157.1	1.36e-17	< 5.35e-15	—	4.63e-18	0.11	1.88e-14	1.02
N[2, 5]b	6564.6	196.0	1.36e-17	< 6.68e-15	—	4.63e-18	< 0.14	1.74e-14	0.27
N[2, 6]a	6155.4	193.5	1.34e-17	< 6.48e-15	—	4.16e-18	< 0.11	2.20e-14	0.76
N[2, 6]b	6816.6	146.6	1.34e-17	< 4.91e-15	—	4.16e-18	< 0.18	9.69e-15	< 0.16
N[2, 7]a	6183.9	147.8	1.45e-17	< 5.38e-15	—	3.81e-18	< 0.15	1.38e-14	0.85
N[2, 7]b	6775.5	77.1	1.45e-17	< 2.81e-15	—	3.81e-18	< 0.21	5.33e-15	0.20
N[2, 8]a	6118.8	143.8	1.82e-17	< 6.56e-15	—	3.87e-18	< 0.10	1.30e-14	0.69
N[3, 1]a	6193.2	151.1	1.38e-17	< 5.23e-15	—	3.84e-18	0.16	1.96e-14	0.83
N[3, 1]b	6683.4	156.0	1.38e-17	< 5.39e-15	—	3.84e-18	0.11	2.31e-14	0.17
N[3, 2]a	6269.4	167.4	1.17e-17	< 4.90e-15	—	4.28e-18	0.11	2.64e-14	0.57
N[3, 2]b	6790.5	134.5	1.17e-17	< 3.94e-15	—	4.28e-18	< 0.07	2.17e-14	0.18
N[3, 3]a	6240.3	196.0	1.36e-17	< 6.68e-15	—	4.11e-18	0.16	3.29e-14	0.61
N[3, 3]b	6816.0	93.3	1.36e-17	< 3.18e-15	—	4.11e-18	0.11	1.99e-14	0.14
N[3, 4]a	6120.6	193.7	1.49e-17	< 7.24e-15	—	4.04e-18	0.16	3.07e-14	0.77
N[3, 4]b	6740.7	138.8	1.49e-17	< 5.19e-15	—	4.04e-18	< 0.07	2.08e-14	0.16
N[3, 5]a	6100.5	150.5	1.15e-17	< 4.35e-15	—	4.33e-18	0.19	2.14e-14	0.91
N[3, 5]b	6594.9	196.0	1.15e-17	< 5.66e-15	—	4.33e-18	< 0.08	2.34e-14	0.28
N[3, 6]a	6199.5	148.3	1.21e-17	< 4.51e-15	—	4.04e-18	0.12	2.07e-14	0.62
N[3, 6]b	6815.7	97.3	1.21e-17	< 2.96e-15	—	4.04e-18	< 0.08	1.16e-14	0.23
N[3, 7]a	6183.9	157.6	1.40e-17	< 5.53e-15	—	4.20e-18	0.08	2.54e-14	0.63
N[3, 7]b	6845.7	95.9	1.40e-17	< 3.36e-15	—	4.20e-18	< 0.07	1.21e-14	0.14
N[3, 8]a	6158.1	115.2	1.54e-17	< 4.44e-15	—	3.29e-18	0.13	1.61e-14	0.88
N[3, 8]b	6671.4	194.7	1.54e-17	< 7.50e-15	—	3.29e-18	< 0.15	1.40e-14	0.33
N[4, 1]a	6305.7	196.0	1.41e-17	< 6.92e-15	—	4.12e-18	< 0.04	3.93e-14	0.52
N[4, 1]b	6750.9	196.0	1.41e-17	< 6.92e-15	—	4.12e-18	0.25	2.32e-14	< 0.09
N[4, 2]a	6240.6	174.1	1.42e-17	< 6.21e-15	—	3.67e-18	0.22	3.29e-14	0.50
N[4, 2]b	6738.0	196.0	1.42e-17	< 6.99e-15	—	3.67e-18	< 0.08	1.90e-14	0.11
N[4, 3]a	6019.2	129.8	1.22e-17	< 3.96e-15	—	3.88e-18	0.23	2.01e-14	1.11
N[4, 3]b	6454.8	196.0	1.22e-17	< 5.99e-15	—	3.88e-18	< 0.05	3.90e-14	0.34
N[4, 4]a	6126.9	196.0	1.28e-17	< 6.27e-15	—	4.14e-18	0.20	5.08e-14	0.62
N[4, 4]b	6770.4	196.0	1.28e-17	< 6.27e-15	—	4.14e-18	< 0.09	2.31e-14	< 0.09
N[4, 5]a	6150.3	185.1	1.49e-17	< 6.90e-15	—	3.64e-18	< 0.08	2.39e-14	0.75
N[4, 5]b	6709.2	196.0	1.49e-17	< 7.30e-15	—	3.64e-18	< 0.15	1.34e-14	0.15
N[4, 6]a	6316.5	196.0	1.43e-17	< 7.03e-15	—	4.97e-18	0.11	3.07e-14	0.49
N[4, 6]b	6879.0	175.9	1.43e-17	< 6.31e-15	—	4.97e-18	< 0.15	1.26e-14	< 0.17
N[4, 7]a	6160.8	151.7	1.31e-17	< 4.97e-15	—	4.04e-18	0.14	2.47e-14	1.03
N[4, 7]b	6528.3	145.3	1.31e-17	< 4.76e-15	—	4.04e-18	< 0.05	2.91e-14	0.22
N[4, 8]a	6229.5	146.9	1.44e-17	< 5.30e-15	—	3.62e-18	< 0.05	2.78e-14	0.77
N[4, 8]b	6675.6	190.9	1.44e-17	< 6.89e-15	—	3.62e-18	< 0.09	1.94e-14	0.14

Table 4. Same as Table 2 for the spaxels of pointing N.

Please give a shorter version with: \authorrunning and/or \titilerunning prior to \maketitle

Spaxel	v_{rad}	σ	$\Sigma_{bkg,blue}$	$f(H\beta)$	$f([OIII]\lambda 5007\text{\AA})$ $/f(H\beta)$	$\Sigma_{bkg,red}$	$f([OI]\lambda 6300\text{\AA})$ $/f(H\alpha)$	$f(H\alpha)$	$f([NII]\lambda 6583\text{\AA})$ $/f(H\alpha)$
N[5, 1]a	6274.8	196.0	1.39e-17	< 6.81e-15	—	4.59e-18	< 0.12	1.74e-14	0.90
N[5, 1]b	6599.7	154.1	1.39e-17	< 5.36e-15	—	4.59e-18	0.22	2.34e-14	0.10
N[5, 2]a	6264.6	196.0	1.49e-17	< 7.33e-15	—	4.40e-18	0.24	1.90e-14	0.79
N[5, 2]b	6543.3	166.6	1.49e-17	< 6.23e-15	—	4.40e-18	< 0.10	1.96e-14	< 0.09
N[5, 3]a	6172.8	161.6	1.40e-17	< 5.68e-15	—	4.24e-18	0.23	2.12e-14	0.74
N[5, 3]b	6634.2	196.0	1.40e-17	< 6.89e-15	—	4.24e-18	< 0.08	2.51e-14	< 0.08
N[5, 4]a	6125.7	196.0	1.56e-17	< 7.68e-15	—	4.46e-18	0.13	2.78e-14	0.74
N[5, 4]b	6633.9	195.6	1.56e-17	< 7.66e-15	—	4.46e-18	< 0.12	2.04e-14	0.15
N[5, 5]a	6010.8	173.8	1.34e-17	< 5.85e-15	—	4.57e-18	0.33	1.35e-14	1.11
N[5, 5]b	6459.9	144.6	1.34e-17	< 4.86e-15	—	4.57e-18	< 0.16	1.03e-14	0.18
N[5, 6]a	6128.1	109.8	1.63e-17	< 4.48e-15	—	4.06e-18	0.41	6.43e-15	1.15
N[5, 6]b	6531.3	174.9	1.63e-17	< 7.13e-15	—	4.06e-18	0.27	1.70e-14	0.31
N[5, 7]a	6208.2	143.8	1.55e-17	< 5.59e-15	—	4.04e-18	0.24	1.32e-14	0.94
N[5, 7]b	6553.8	119.8	1.55e-17	< 4.66e-15	—	4.04e-18	0.11	1.50e-14	0.27
N[5, 8]	—	—	—	—	—	—	—	—	—
N[6, 1]a	5802.9	< 16.7	1.47e-17	-8.92e-16	< 1.50	4.10e-18	< 0.04	-4.20e-15	0.44
N[6, 1]b	6399.3	196.0	1.47e-17	< 7.21e-15	—	4.10e-18	0.10	2.43e-14	0.42
N[6, 2]a	6421.2	133.2	1.38e-17	< 4.60e-15	—	4.07e-18	0.14	2.72e-14	0.52
N[6, 3]a	6103.8	129.1	1.46e-17	< 4.72e-15	—	3.77e-18	< 0.14	9.29e-15	0.90
N[6, 3]b	6452.1	119.2	1.46e-17	< 4.36e-15	—	3.77e-18	0.32	1.83e-14	0.19
N[6, 4]a	6277.5	196.0	1.40e-17	< 6.87e-15	—	5.03e-18	0.16	2.01e-14	0.72
N[6, 4]b	6724.5	129.3	1.40e-17	< 4.53e-15	—	5.03e-18	< 0.10	1.01e-14	< 0.16
N[6, 5]a	5935.5	98.4	1.53e-17	< 3.79e-15	—	4.56e-18	< 0.12	8.67e-15	0.64
N[6, 5]b	6525.3	196.0	1.53e-17	< 7.54e-15	—	4.56e-18	< 0.14	1.45e-14	< 0.15
N[6, 6]a	6018.6	110.5	1.46e-17	< 4.05e-15	—	3.75e-18	< 0.14	7.91e-15	0.80
N[6, 6]b	6564.9	166.4	1.46e-17	< 6.10e-15	—	3.75e-18	< 0.17	1.04e-14	0.39
N[6, 7]a	6110.7	99.1	1.56e-17	< 3.88e-15	—	4.40e-18	0.33	5.47e-15	0.92
N[6, 7]b	6572.4	156.2	1.56e-17	< 6.11e-15	—	4.40e-18	< 0.14	1.34e-14	0.30
N[6, 8]a	6613.5	71.7	1.64e-17	< 2.96e-15	—	4.32e-18	< 0.09	6.99e-15	0.23
N[7, 1]	—	—	—	—	—	—	—	—	—
N[7, 2]a	6297.0	178.5	1.89e-17	< 8.45e-15	—	5.43e-18	< 0.14	1.69e-14	0.47
N[7, 3]a	6258.9	167.0	1.64e-17	< 6.88e-15	—	4.23e-18	< 0.11	1.74e-14	0.70
N[7, 4]a	6302.4	196.0	1.45e-17	< 7.12e-15	—	5.17e-18	0.41	1.28e-14	0.44
N[7, 5]a	6754.5	105.5	1.61e-17	< 4.27e-15	—	4.37e-18	< 0.16	6.38e-15	< 0.18
N[7, 6]	—	—	—	—	—	—	—	—	—
N[7, 7]a	6612.6	167.3	1.51e-17	< 6.35e-15	—	3.08e-18	< 0.26	8.03e-15	0.51
N[7, 8]a	6653.4	81.9	1.44e-17	< 2.95e-15	—	4.46e-18	< 0.15	6.44e-15	0.35
N[8, 1]a	6074.4	60.2	1.86e-17	< 2.81e-15	—	4.14e-18	< 0.15	3.62e-15	< 0.17
N[8, 2]a	6140.1	100.0	1.94e-17	< 4.86e-15	—	4.30e-18	< 0.12	7.88e-15	0.94
N[8, 3]a	6135.6	85.9	1.68e-17	< 3.63e-15	—	5.36e-18	< 0.12	6.74e-15	1.14
N[8, 4]	—	—	—	—	—	—	—	—	—
N[8, 5]	—	—	—	—	—	—	—	—	—
N[8, 6]	—	—	—	—	—	—	—	—	—
N[8, 7]a	6617.4	90.5	1.59e-17	< 3.60e-15	—	4.29e-18	< 0.19	5.45e-15	< 0.18
N[8, 8]a	6674.4	68.4	1.85e-17	< 3.17e-15	—	4.22e-18	< 0.14	5.49e-15	< 0.13

Table 4. Continued.

Spaxel	$12 + \log O/H$ (O3N2)
S[2,2]	8.50
S[2,3]	8.50
S[5,2]	8.45
M[2,2]	8.61

Table 5. Oxygen abundances for the brightest spaxels showing H γ -like spectra in pointings S and M, estimated following the Pettini & Pagel (2004) method, using the $([OIII]\lambda 5007\text{\AA}/H\beta)/([NII]\lambda 6583\text{\AA}/H\alpha)$ (O3N2) indicator.

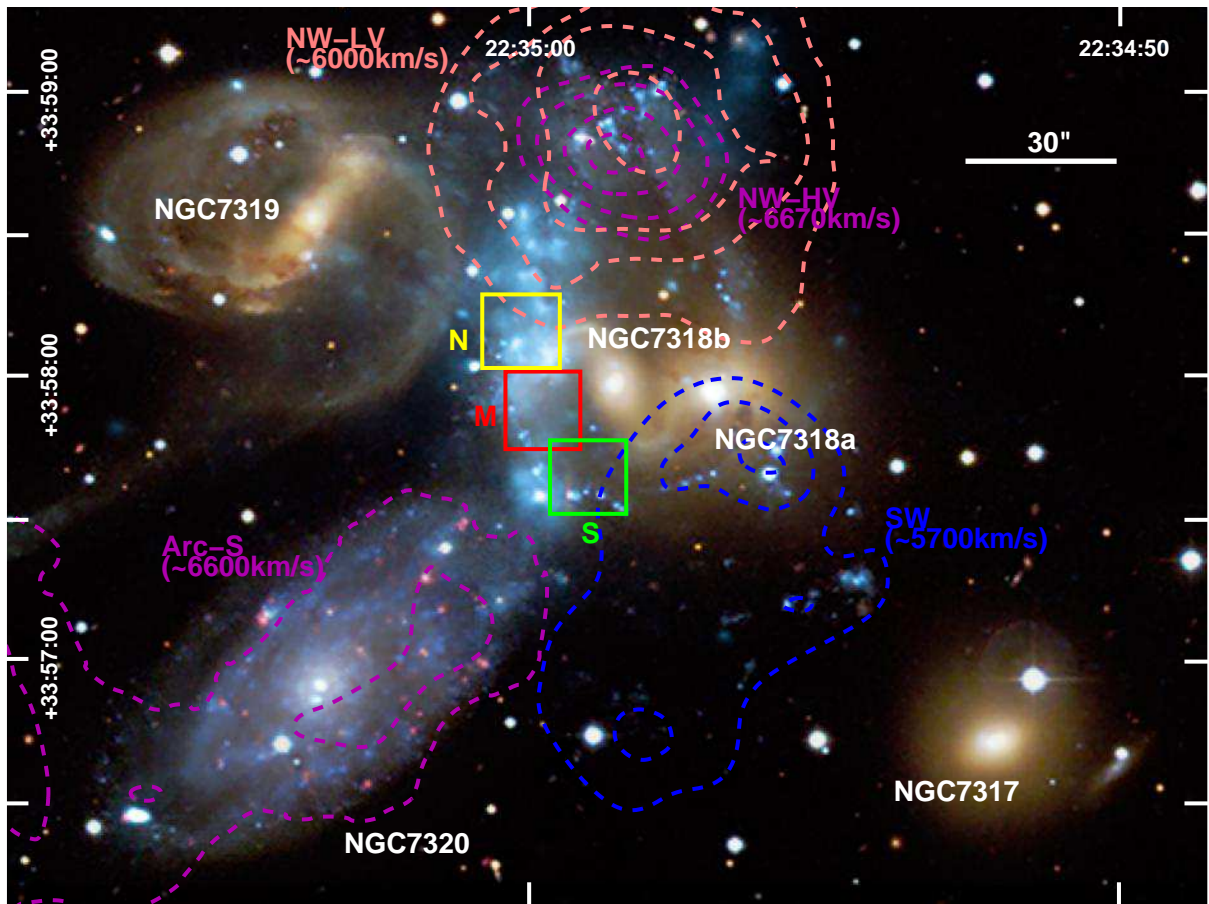


Fig. 1. False color image of SQ. The color code is as follows: X-ray from CHANDRA (cyan), optical light (red, yellow, blue and white) from the CFHT. The image width is 6.3 arcmin. North is up. Overimposed we show our three PMAS pointings (yellow, red and green for the N, M and S pointings respectively). We also overlaid the H α contours from Williams et al. (2002) and labeled the four main structures reported in that paper as well as their approximate recession velocities. The bar representing an angular distance of 30" corresponds to a linear scale of 12.89 kpc.

Pointing S

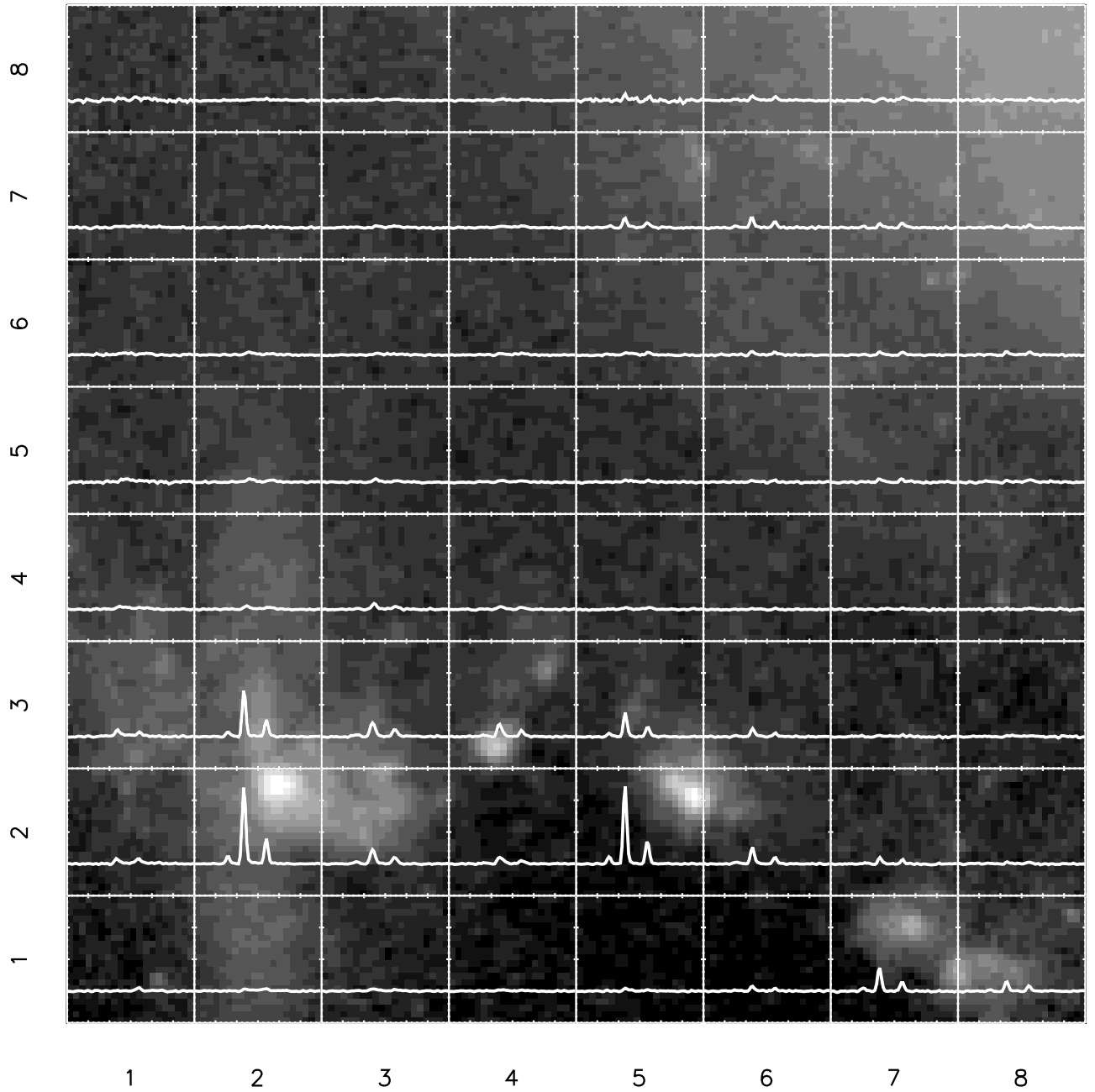


Fig. 2. Spatial arrangement of the spectra of pointing S after a 2×2 binning of the spaxels overlaid on the HST V-band image. The X-axis of all spectra ranges from 6650\AA to 6750\AA . The Y-axis scale is the same for all the spectra and ranges from -1.53×10^{-17} to $1.53 \times 10^{-16} \text{ erg s}^{-1} \text{ cm}^{-2} \text{ \AA}^{-1}$. Each spectrum is univocally identified by two numbers indicating the row and column occupied in the two dimensional array. The orientation of the array is such that North is up and East is left.

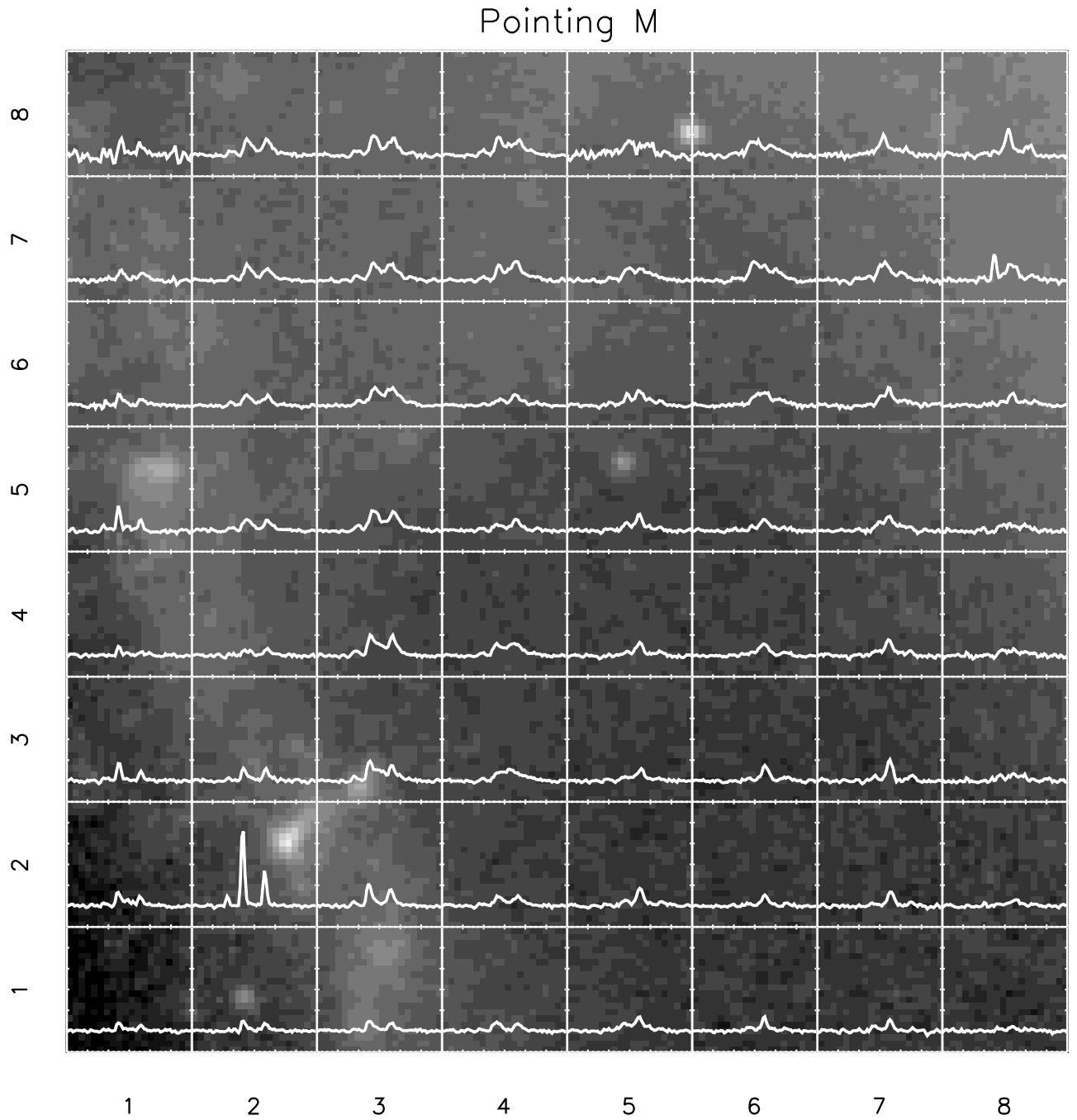


Fig. 3. Same as Figure 2 for pointing M. The Y-axis scale is the same for all the spectra and ranges from -4.39×10^{-17} to 4.39×10^{-16} erg s $^{-1}$ cm $^{-2}$ Å $^{-1}$.

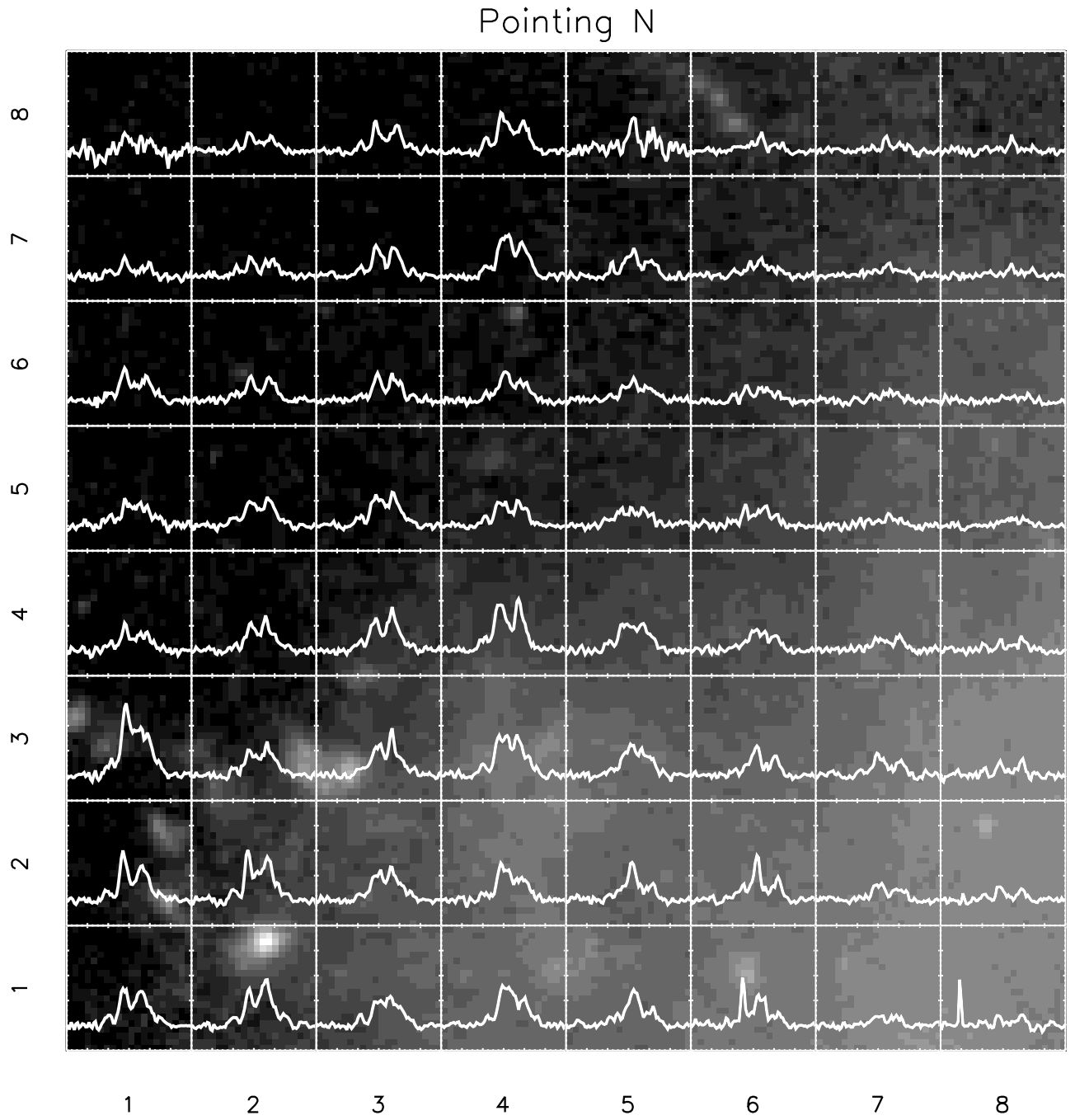


Fig. 4. Same as Figure 2 for pointing N. The Y-axis scale is the same for all the spectra and ranges from -1.53×10^{-17} to $1.53 \times 10^{-16} \text{ erg s}^{-1} \text{ cm}^{-2} \text{ \AA}^{-1}$.

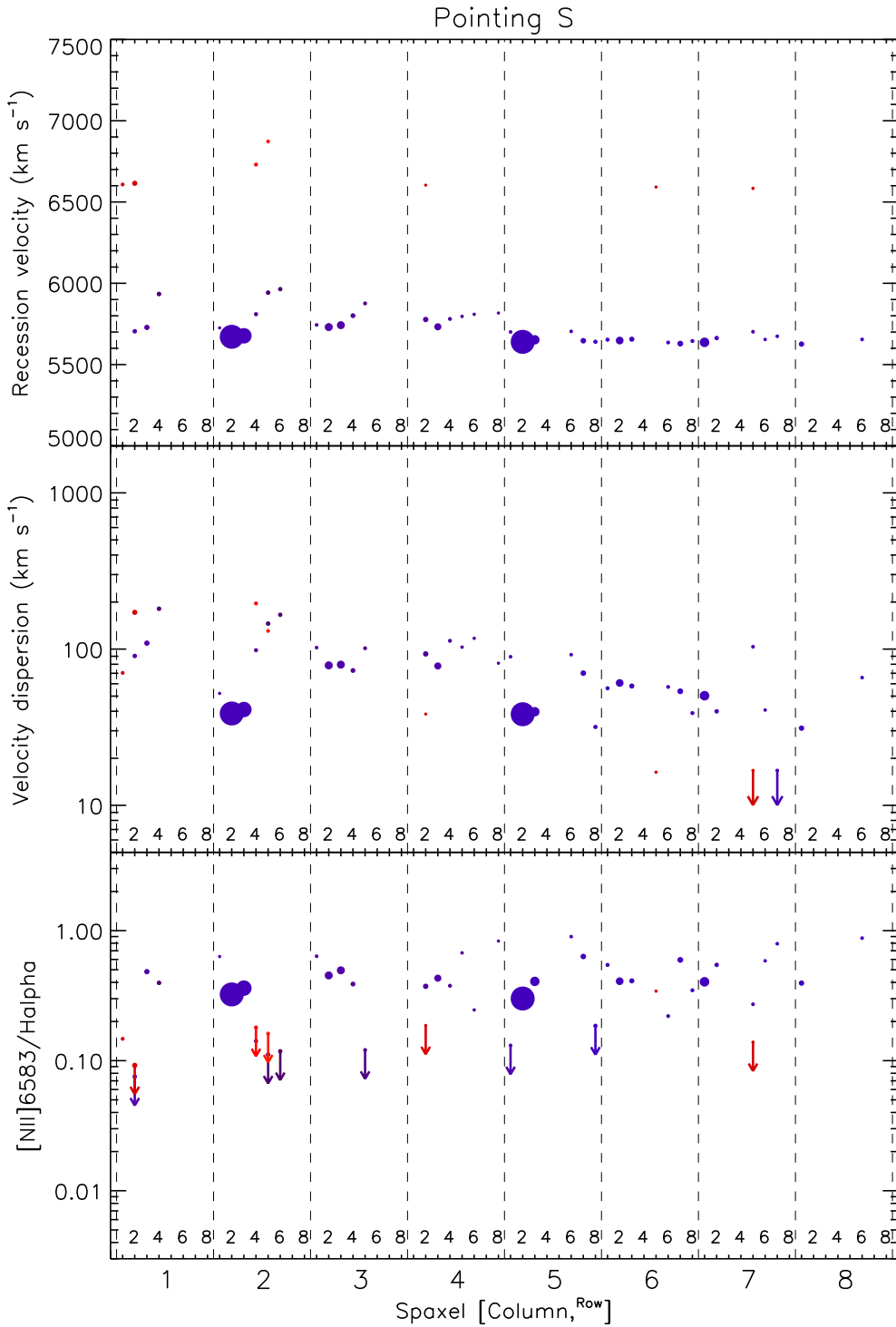


Fig. 5. Recession velocity (top), velocity dispersion (middle) and [NII] λ 6583 \AA /H α flux ratio (bottom) for the spectra of pointing S. Arrows correspond to upper limits in [NII] λ 6583 \AA /H α and σ . Only components for which the intensity peak of the H α line is above $5\Sigma_{\text{bkg}}$ are plotted. The major and minor ticks of the X-axis correspond to the column and the row of each spaxel respectively as it is illustrated in Figures 2 to 4. For each spectrum, each component is represented for a filled dot. In the three panels, the color of the dots is related to the recession velocity of the component, where bluer corresponds to lower velocity, and redder corresponds to higher velocity, and the size of each dot is proportional to the flux of the H α line of the corresponding component.

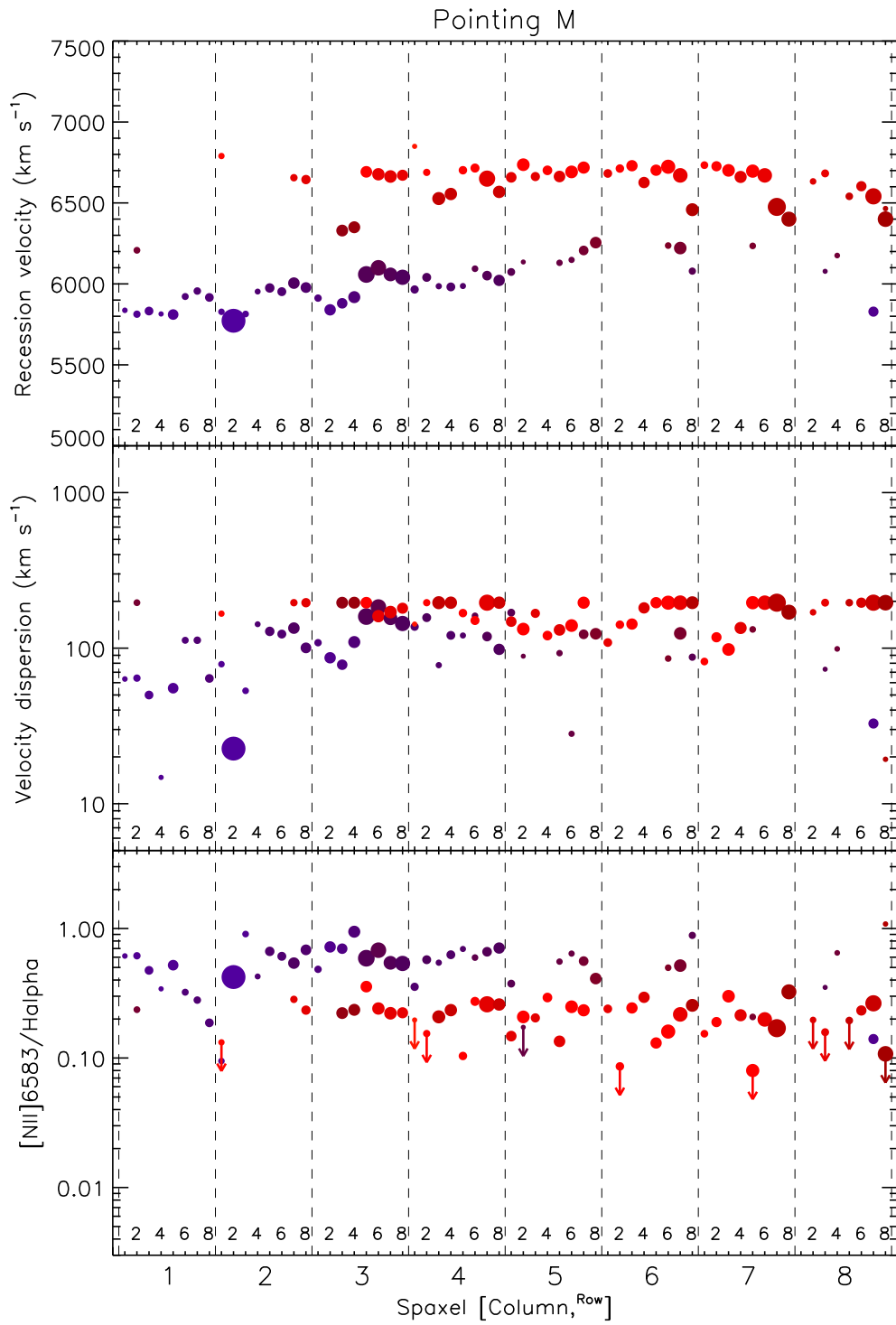


Fig. 6. Same as Figure 5 for pointing M.

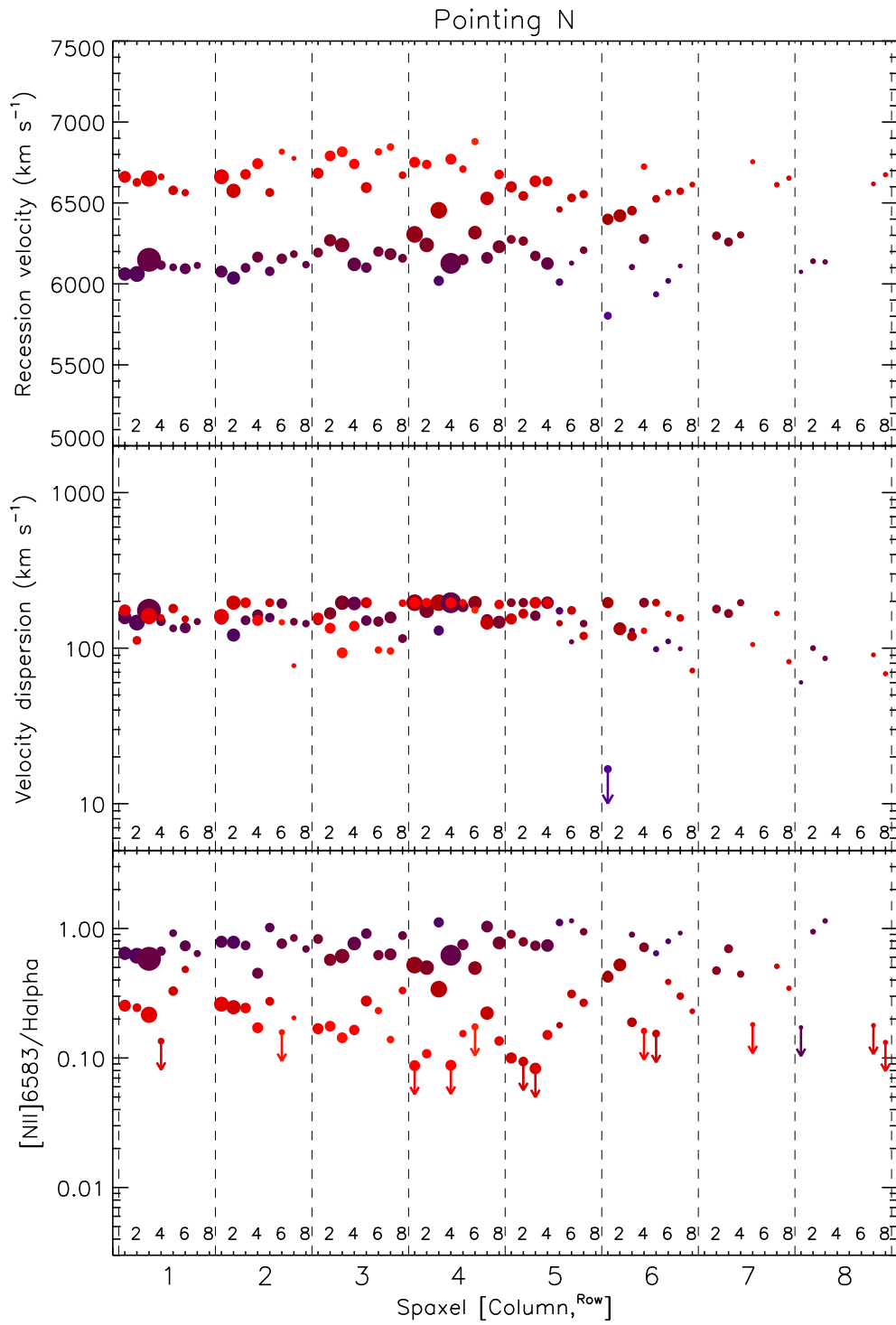


Fig. 7. Same as Figure 5 for pointing N.

Please give a shorter version with: \authorrunning and/or \titilerunning prior to \maketitle

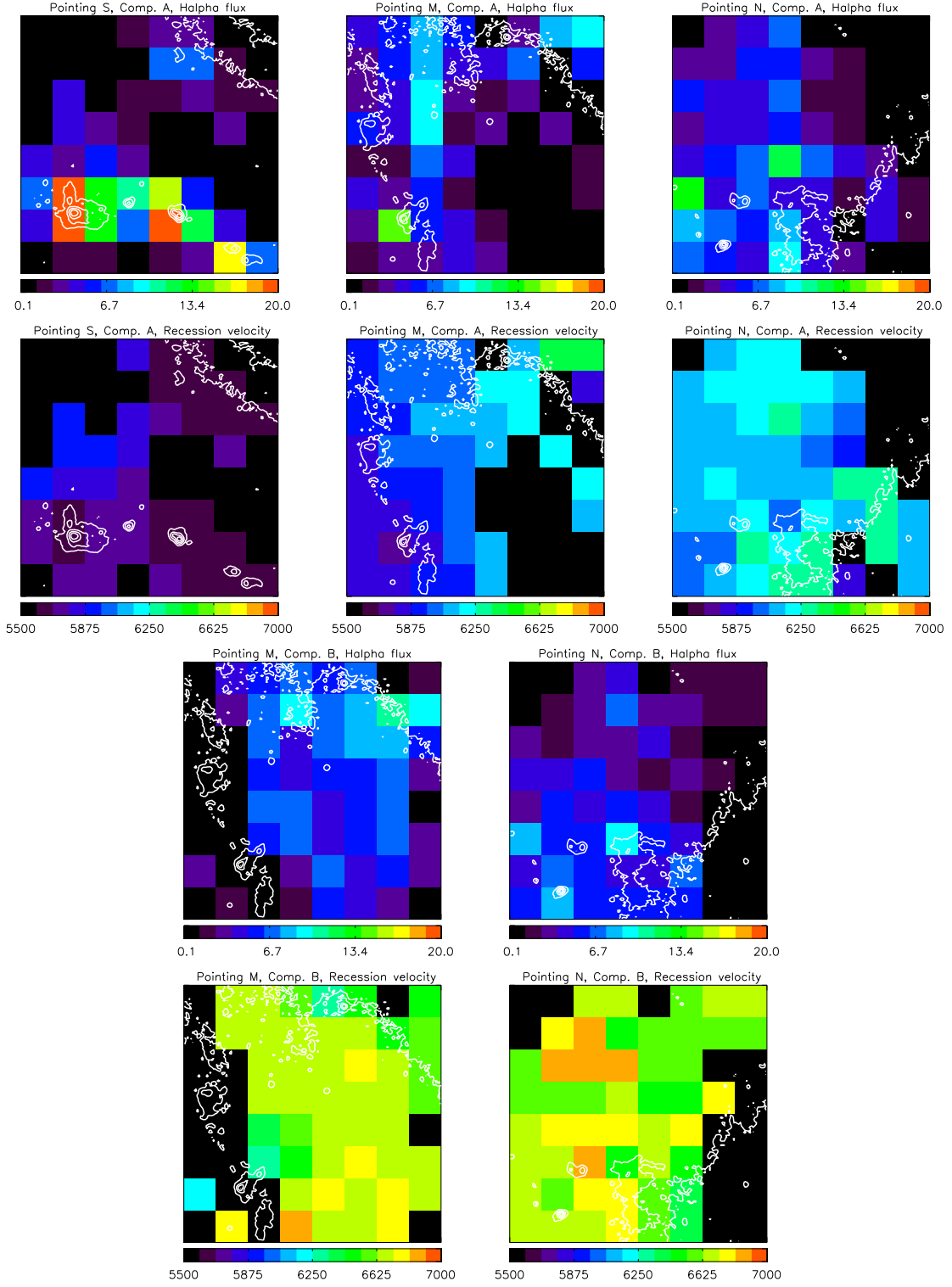


Fig. 8. First row: H α flux maps of component A corresponding to pointings S (left), M (middle) and N (right), in units of 10^{-16} erg s $^{-1}$ cm $^{-2}$. Second row: Radial velocity maps of component A corresponding to pointings S (left), M (middle) and N (right), in units of km s $^{-1}$. Third row: H α flux maps of component B corresponding to pointings M (left) and N (right), in units of 10^{-16} erg s $^{-1}$ cm $^{-2}$. Fourth row: Radial velocity maps of component B corresponding to pointings M (left) and N (right), in units of km s $^{-1}$. White contours correspond to the V-band HST image: 18.99, 18.23, 17.48 and 16.73 mag arcsec $^{-2}$. North is up, East is left.

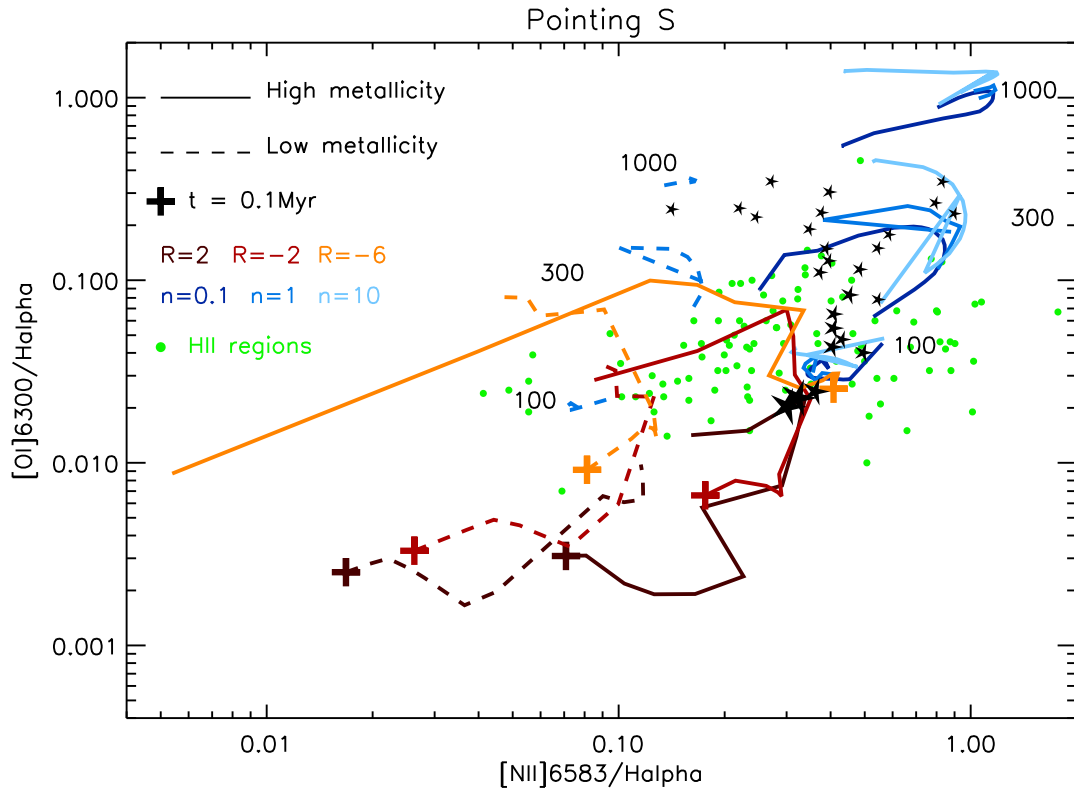


Fig. 9. $[\text{NII}]\lambda 6583\text{\AA}/\text{H}\alpha$ vs. $[\text{OI}]\lambda 6300\text{\AA}/\text{H}\alpha$ for the spaxels of pointing S. Black stars and dots correspond to components A and B respectively. The size of the dots is proportional to the flux of the $\text{H}\alpha$ line. Only components for which the intensity peaks of the lines $[\text{OI}]\lambda 6300\text{\AA}$ and $[\text{NII}]\lambda 6583\text{\AA}$ are above Σ_{bkg} are plotted. The brown lines correspond to the star formation models from Dopita et al. (2006) (solid lines for solar metallicity and dashed lines for 0.4 solar metallicity). Each line corresponds to a temporal sequence where the beginning is indicated with a '+' and corresponds to an age of $t = 0.1$ Myr, and the opposite tip of the line corresponds to an age of $t = 6$ Myr. The values of the parameter R are color coded as indicated in the legend. The blue lines correspond to the shock+precursor models of Allen et al. (2008) (solid lines for solar metallicity and dashed lines for SMC metallicity). The values of the pre-shock density are color coded and indicated in the legend in units of cm^{-3} . For SMC metallicity only models with $n_e = 1 \text{ cm}^{-3}$ are plotted. The numbers close to the shock models indicate the shock velocity in km s^{-1} . Small green dots correspond to the samples of H II regions from van Zee et al. (1998) and van Zee & Haynes (2006).

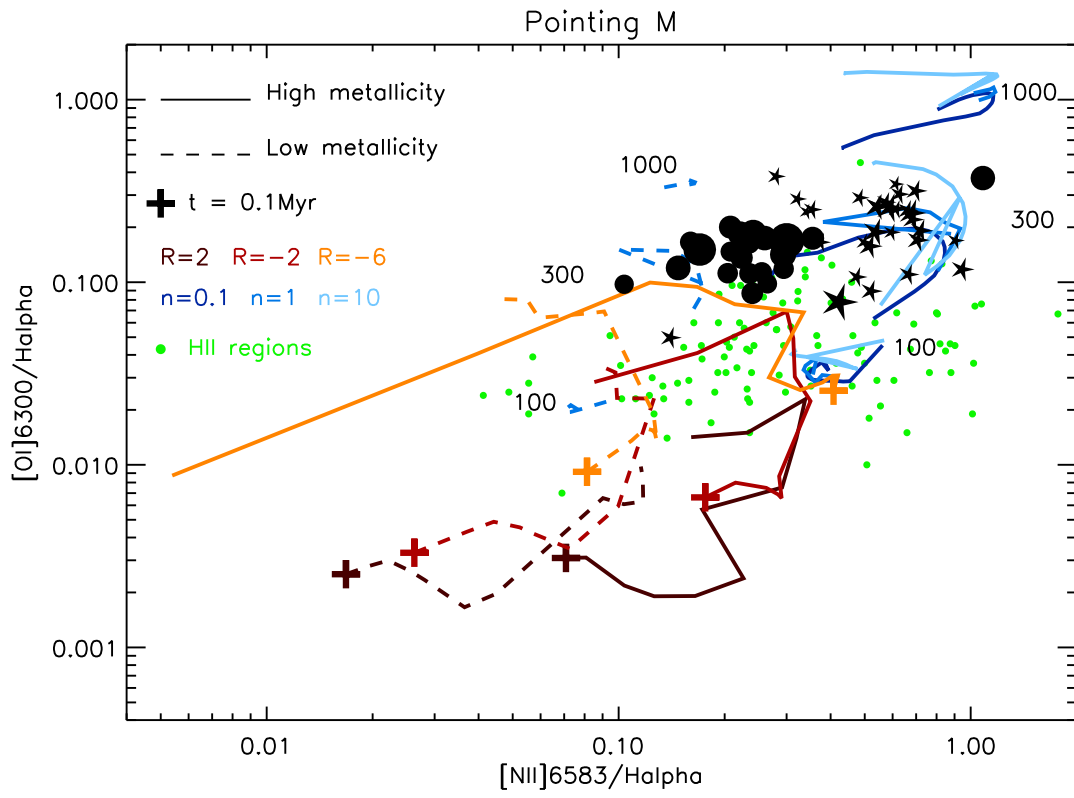


Fig. 10. Same as Figure 9 for pointing M.

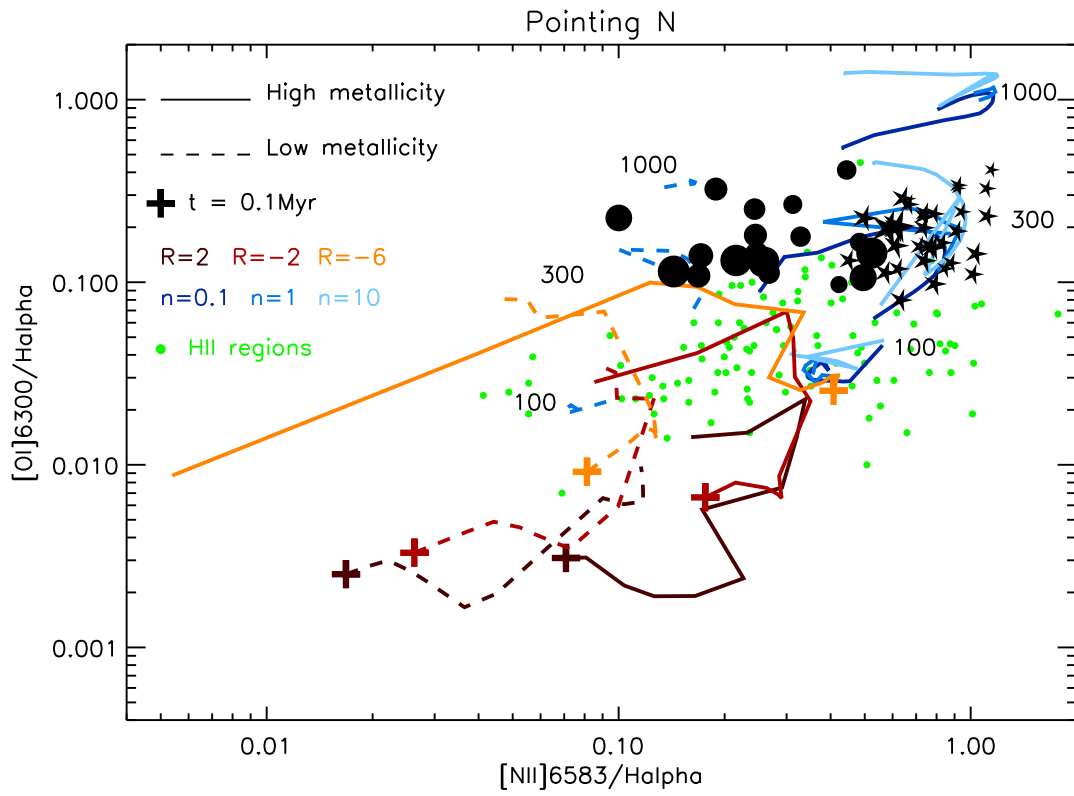


Fig. 11. Same as Figure 9 for pointing N.

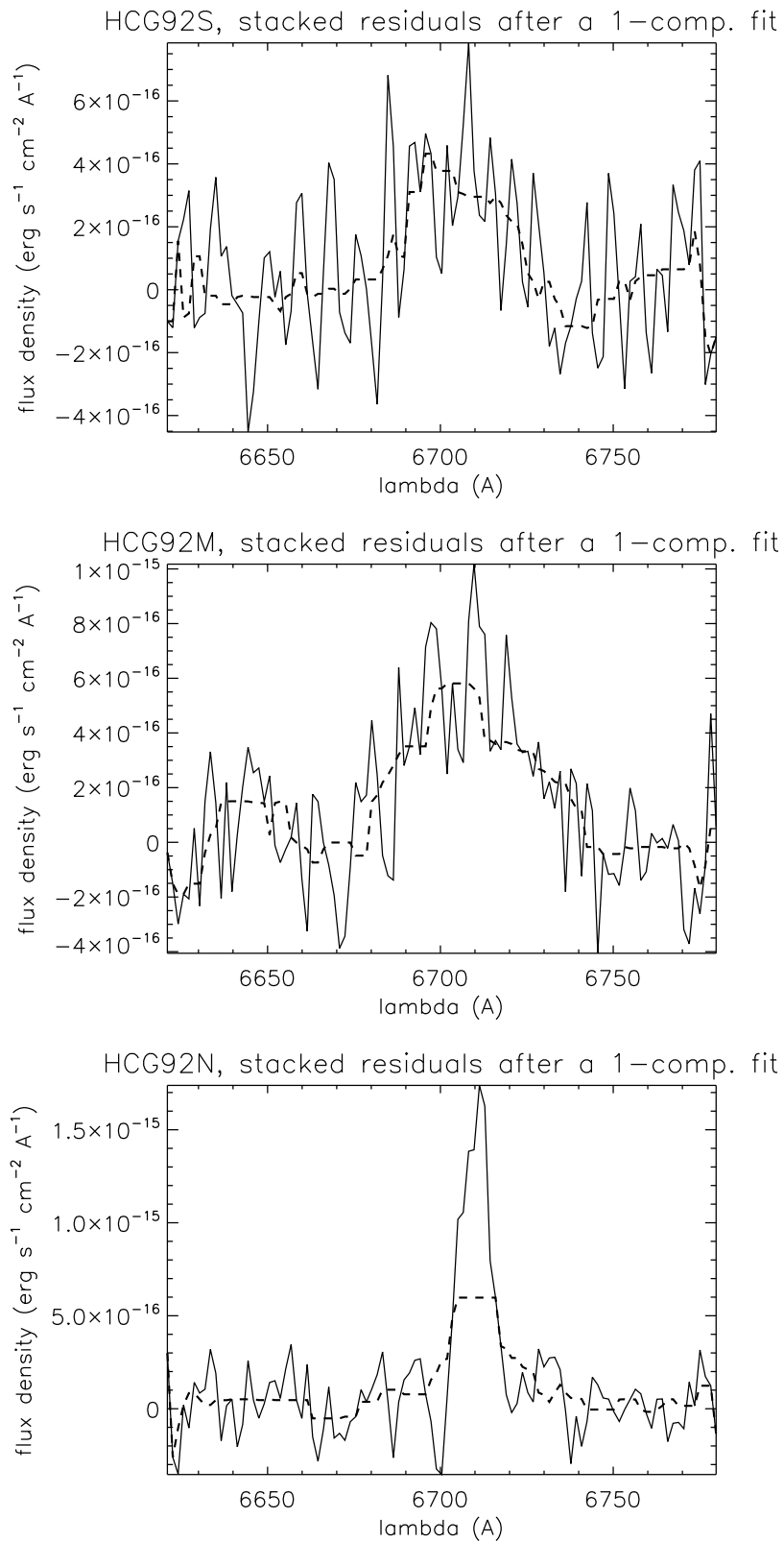


Fig. 12. Stacked residuals of the 64 spaxels of the three pointings after a 1-component fit. The dashed line corresponds to the median along 15 pixels in the X-axis.

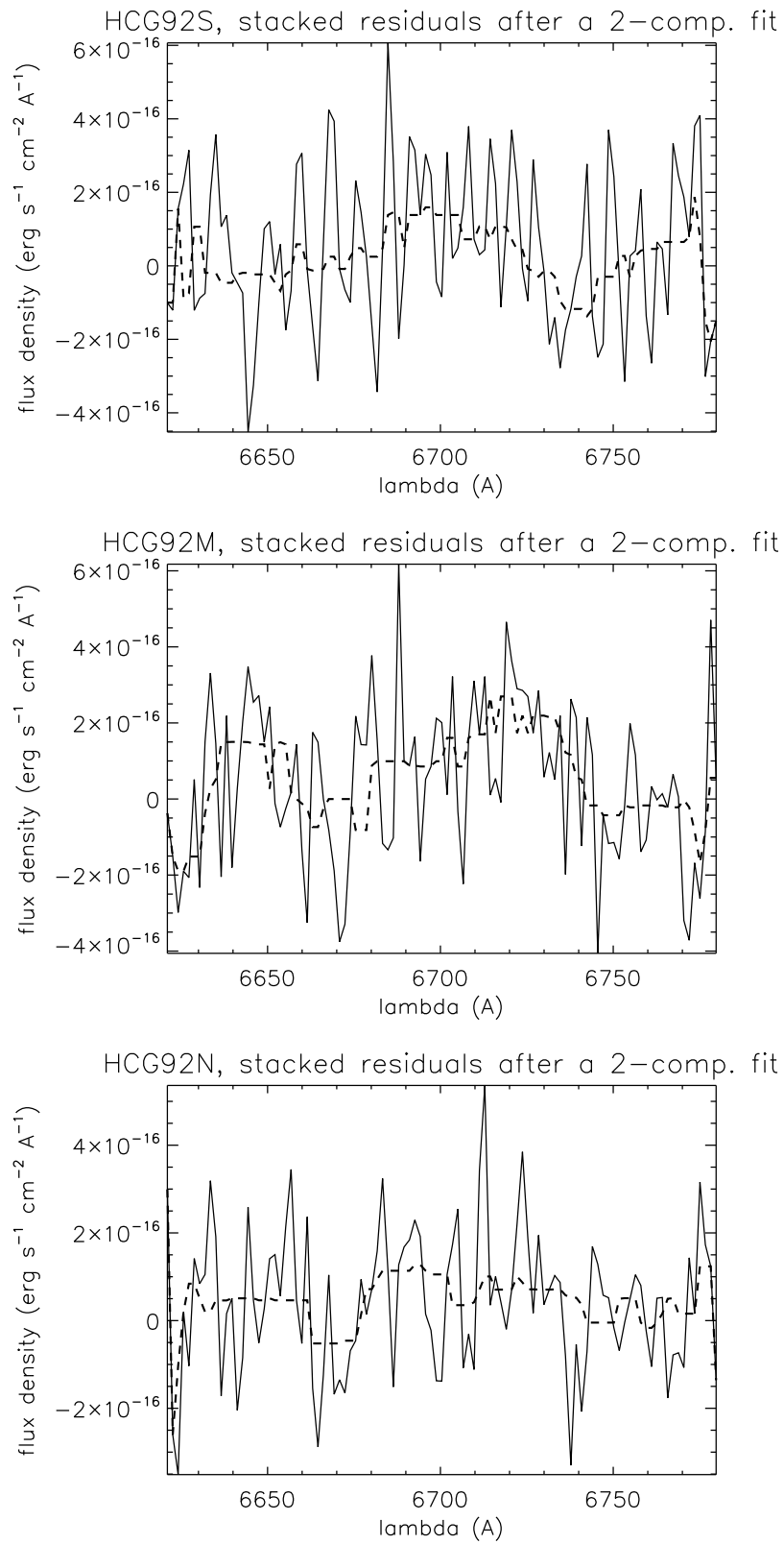


Fig. 13. Stacked residuals of the 64 spaxels of the three pointings after a 2-component fit. The dashed line corresponds to the median along 15 pixels in the X-axis.

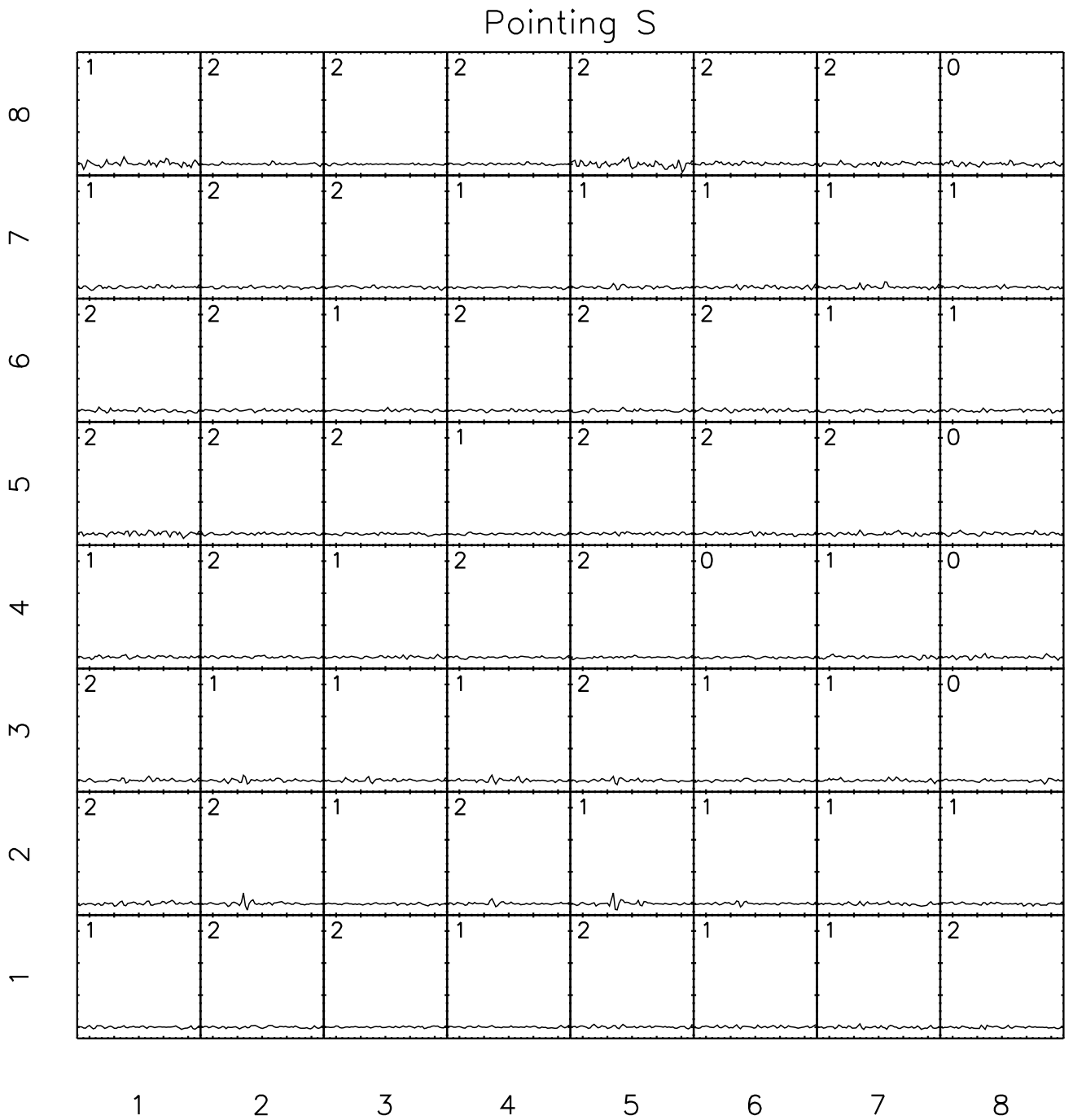


Fig. 14. Spatial arrangement of the residua after the fitting procedure of pointing S. The horizontal axis of all spectra ranges from 6650Å to 6750Å. The vertical axis scale is the same as in Figure 2. The number to the top left corner of each panel indicates the number of components resulting from the fitting procedure. A spaxel labeled with '0' means that 0 components were assigned to this spaxel.

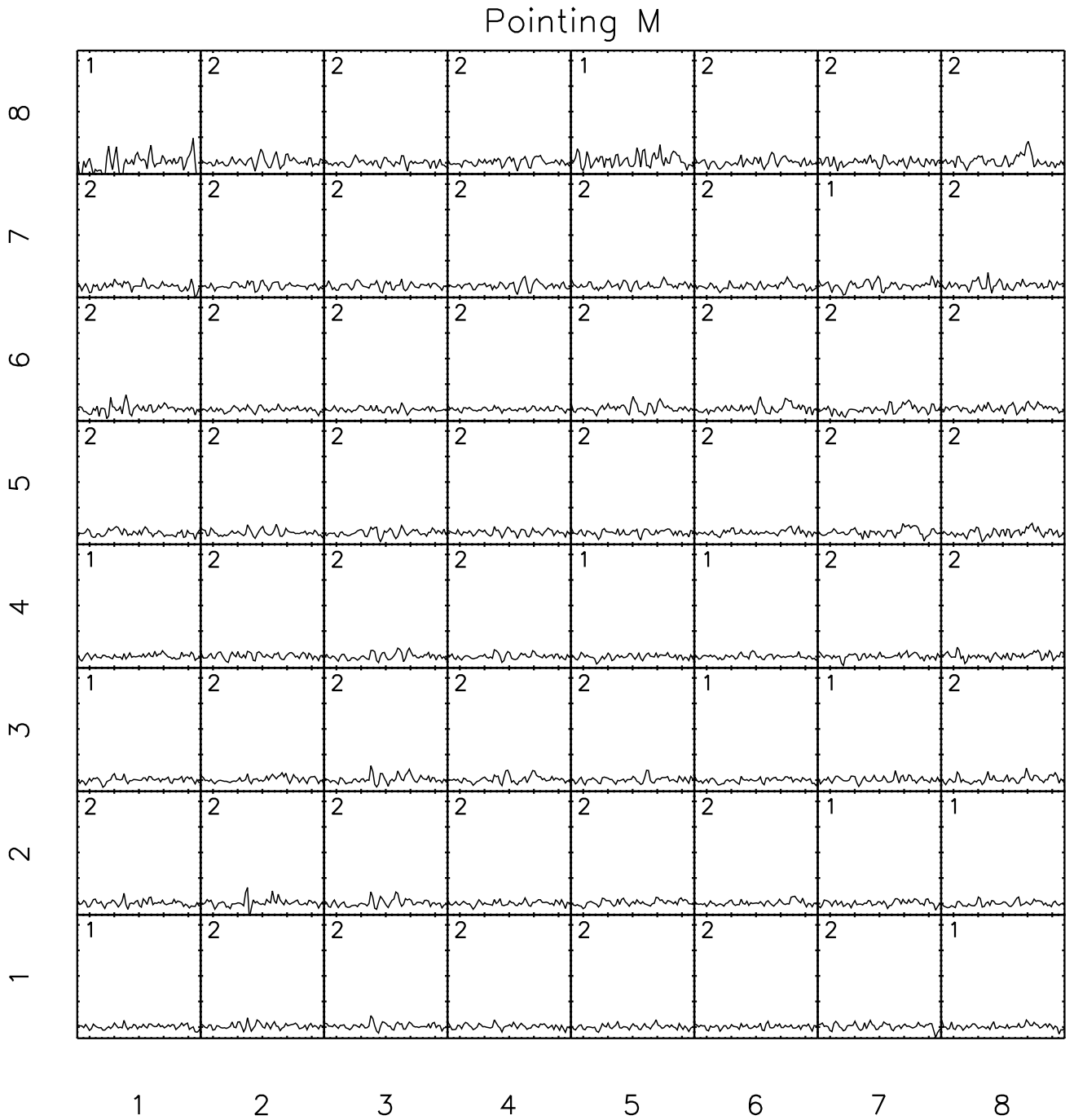


Fig. 15. Spatial arrangement of the residua after the fitting procedure of pointing S. The horizontal axis of all spectra ranges from 6650Å to 6750Å. The vertical axis scale is the same as in Figure 3. The number to the top left corner of each panel indicates the number of components resulting from the fitting procedure. A spaxel labeled with '0' means that 0 components were assigned to this spaxel.

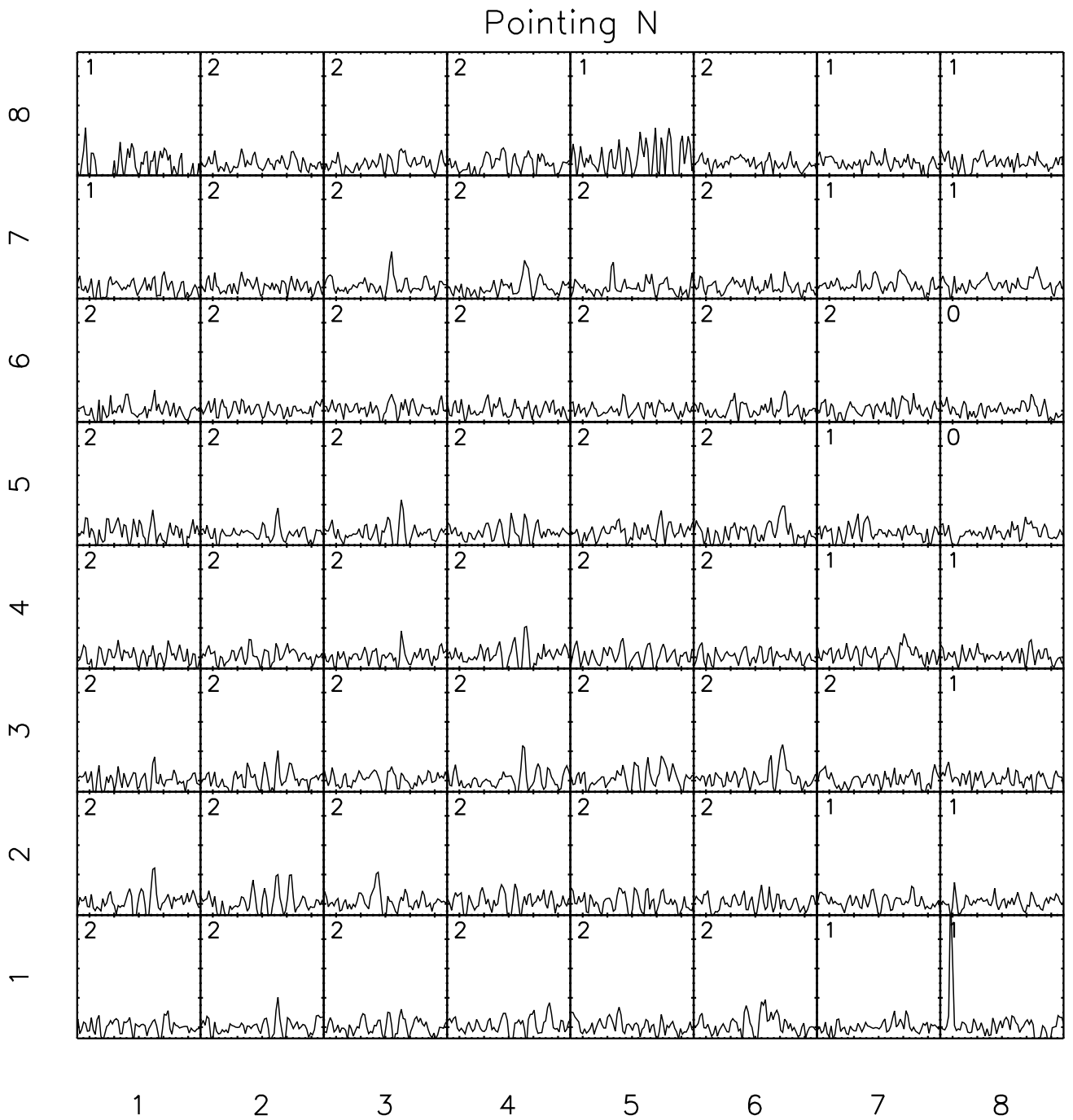


Fig. 16. Spatial arrangement of the residua after the fitting procedure of pointing S. The horizontal axis of all spectra ranges from 6650Å to 6750Å. The vertical axis scale is the same as in Figure 4. The number to the top left corner of each panel indicates the number of components resulting from the fitting procedure. A spaxel labeled with '0' means that 0 components were assigned to this spaxel.

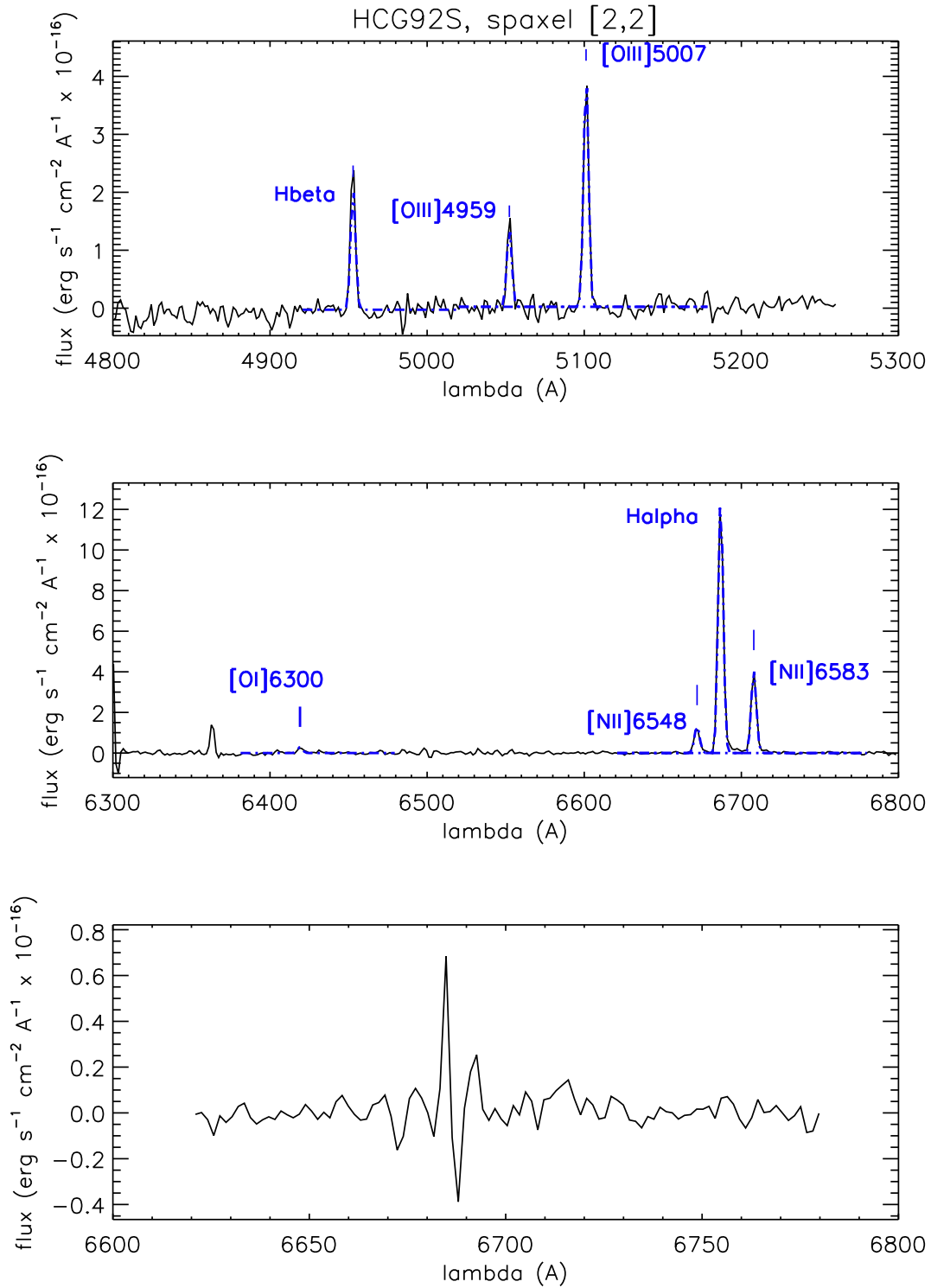


Fig. 17. Top: Blue spectrum of spaxel S[2,2]; Middle: Red spectrum of spaxel S[2,2]. Bottom: Residua of the best fit to the spectrum of spaxel S[2,2] in the red wavelength range. The best fit to the emission lines of components A and B for which the intensity peak is above Σ_{bkg} are shown in blue and red respectively.

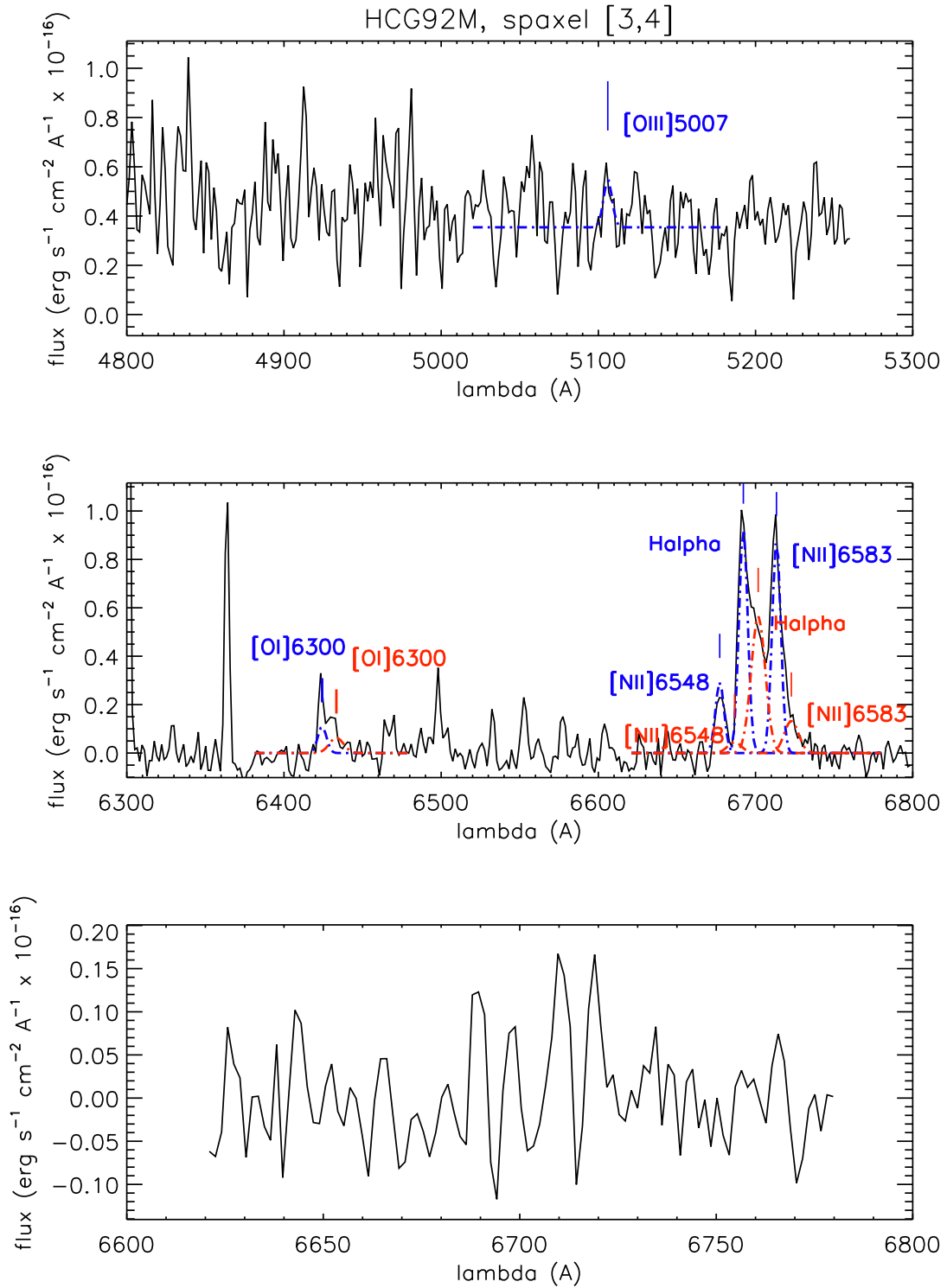


Fig. 18. Same as figure 17 for spaxel M[3,4].

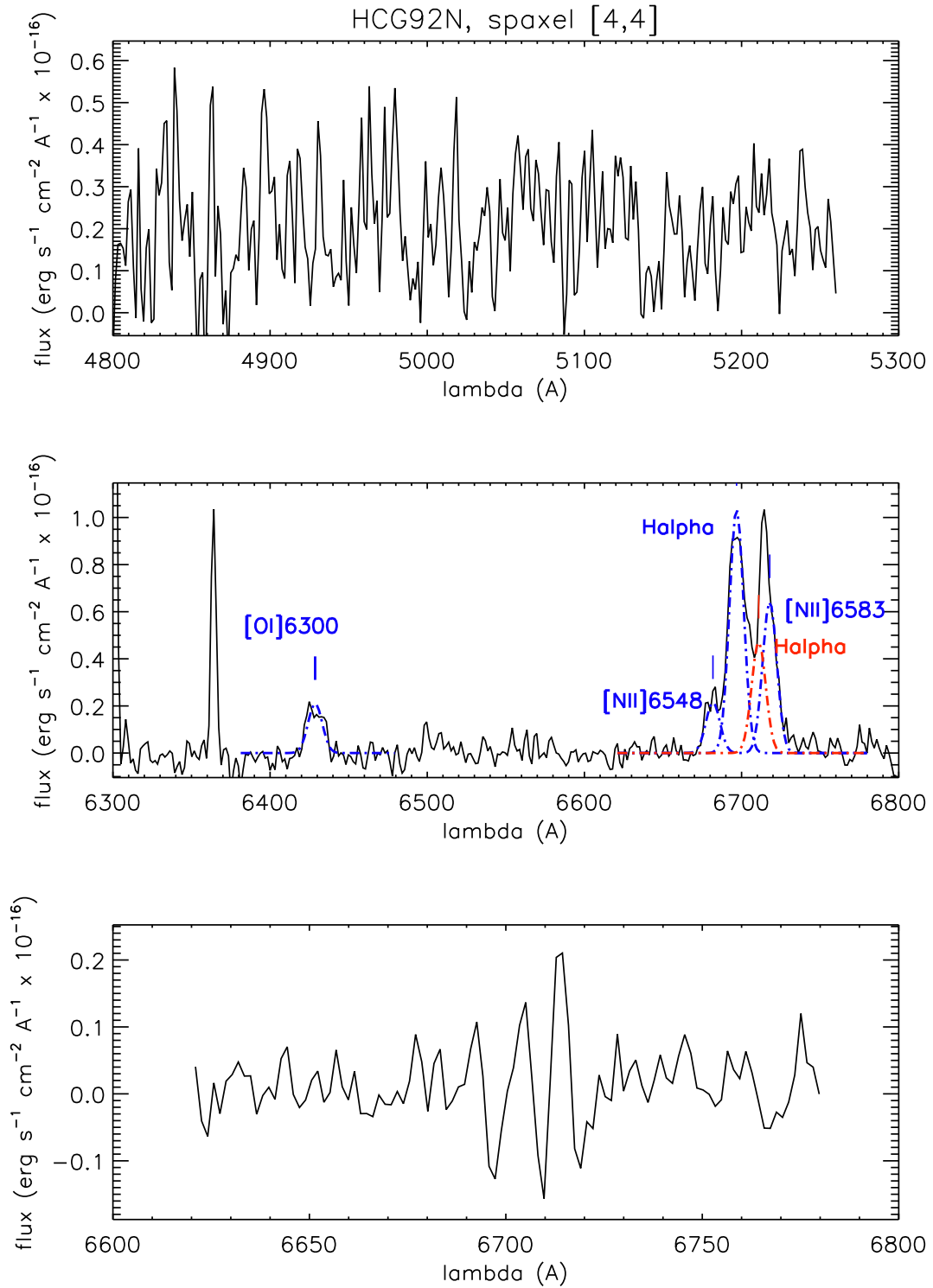


Fig. 19. Same as figure 17 for spaxel N[4,4].